# A Practical, Direct Approach for Fusion of Tool Size Measurement and Flank Wear Prediction of End-Mills in Machining

Haibo Feng

A Thesis

in

The Department

of

Mechanical, Industrial, and Aerospace Engineering

Presented in Partial Fulfillment of the Requirements

for the Degree of

Master of Applied Science (Mechanical Engineering) at

Concordia University

Montreal, Quebec, Canada

August 2022

**CONCORDIA UNIVERSITY**

**School of Graduate Studies**

This is to certify that the thesis prepared

By: **Haibo Feng**

Entitled: **A Practical, Direct Approach for Fusion of Tool Size Measurement and Flank Wear Prediction of End-Mills in Machining**

and submitted in partial fulfillment of the requirements for the degree of Master of

**Master of Applied Science (Mechanical Engineering)**

complies with the regulations of the University and meets the accepted standards with respect to originality and quality.

Signed by the final Examining Committee:

Dr. Mingyuan Chen Chair

Dr. Mingyuan Chen Examiner

Dr. Yong Zeng Examiner

Dr. Zezhong Chen Supervisor

Approved by Dr. Martin Pugh
Chair of Department or Graduate Program Director

Dr. Mourad Debbabi
Dean of Faculty

Date August 19, 2022

# Abstract

A Practical, Direct Approach for Fusion of Tool Size Measurement and Flank Wear Prediction of End-Mills in Machining

Haibo Feng

On-machine measurement (OMM) of cutting tools is to automatically and directly measure them for length and diameter in machining breaks and compensated tool paths in the following machining. Tool condition monitoring (TCM) is to automatically predict tool wear and detect tool failure in machining, which is often evaluated with the width of flank wear land. OMM of cutting tools is widely applied with tool setters in the industry, however, it cannot measure flank wear to monitor tool conditions and predict the tool life. To address the problem in this research, an approach for fusion of tool size measurement and flank wear prediction of end-mills is proposed. First, the model of a fillet end-mill is built. Design principles are studied based on practical machining, which include the smoothness of the end-mill's flank face, and the relief angle of the fillet cutting edge. Second, the model of an indexable face mill is also built accurately. Third, the geometric relationship between tool radius and flank wear land width is established for the indexable face mill. Then, an experimental method is adopted to optimize measurement locations. At last, experiments are conducted that the end-mill is measured at the locations, and the tool radius is used to calculate the flank wear width. The results show the proposed approach is effective for tool condition monitoring. This research successfully develops the OMM-TCM fusion technology and benefits the manufacturing industry.

# Acknowledgments

I hereby express my sincere gratitude to my supervisor, Dr. Chevy Chen, for his constant guidance and encouragement in leading me through the thesis. He has always been generous in offering valuable suggestions, answering my questions, and discussing with me. His keen and meticulous academic observation enlightens me on this thesis and my future study. Dr. Chevy Chen is also a mentor in my life, helping me become more responsible, intelligent, and thoughtful.

Besides, I would like to thank my fellows in our lab. They provide me with a wonderful learning environment and share their knowledge with me when I face difficulties with the research. I also owe my appreciation to my friends, who gave me a lot of care and inspiration during my study in Concordia.

Last but not least, I am deeply in debt to my parents, for their support from the very beginning of my study. Their unwavering love is always the driving power of my work.

# Table of Contents

# List of Figures

# List of Tables

# Chapter 1 Introduction

## 1.1 Background

In modern manufacturing, computer numerical control (CNC) machining occupies an important position due to its high accuracy and high efficiency. The combination of machining and measuring has become mainstream. It provides a monitoring environment to guarantee the accuracy of the machined parts, which generates plenty of advanced measurement techniques. On-machine measurement (OMM) for cutting tools is applied in the industry with tool setters to measure the tool radius and length in machining. It avoids manual measurement interventions and provides a high level of convenience and security. However, tool wear occurs in any cutting process and the amount of tool wears increases gradually, directly affecting the tool life. The reduction of tool radius and length measured by on-machine techniques cannot reflect the actual wear condition of cutting tools. Carrying on the machining process with a worn tool will increase the friction between the tool and the workpiece, leading to a low machining quality. Hence to improve the machining quality, on the other hand, tool condition monitoring (TCM) is also crucial. It's become more necessary to monitor the tool wear and predict the tool life more accurately.

On-machine measurement of cutting tools is to automatically measure the tool radius and length in machining breaks with a tool setter on the machine table. Tool paths are compensated in the following machining with the reduction of tool radius and length. Figure 1.1 shows a laser tool setter widely applied in the on-machine measurement system. It can successfully perform tool measurement without unloading the tool from the CNC machine, and update the tool size data in the CNC controller before it is used to continue cutting the workpiece [1-2].

Tool condition monitoring is to automatically measure tool wear and detect tool failure in machining. It has become essential to machine highly accurate parts and achieves cost-effective machining. In machining a workpiece on a CNC machine, the cutting tool wears out over time in different forms. Tribology classifies tool wear into six forms: flank wear, chipping on cutting edge, crater, build-up-edge, notch, and plastic deformation [3]. A cutter wears out in one or more forms; when the tool wear is too large, it is defective and needs replacing immediately. Therefore, the tool wear is closely related to tool life [4-5]. Flank wear is the most popular wear (see Fig. 1.2), and it is caused by friction between the flank face and the machined surfaces, resulting in cutting-edge depletion and poor part-surface finish [6]. Meanwhile, the flank wear measurement is also used to analyze and describe the durability and lifetime of cutting tools [7]. The TCM requires measuring flank wear in machining [8], contributing to the tool-life prediction development.

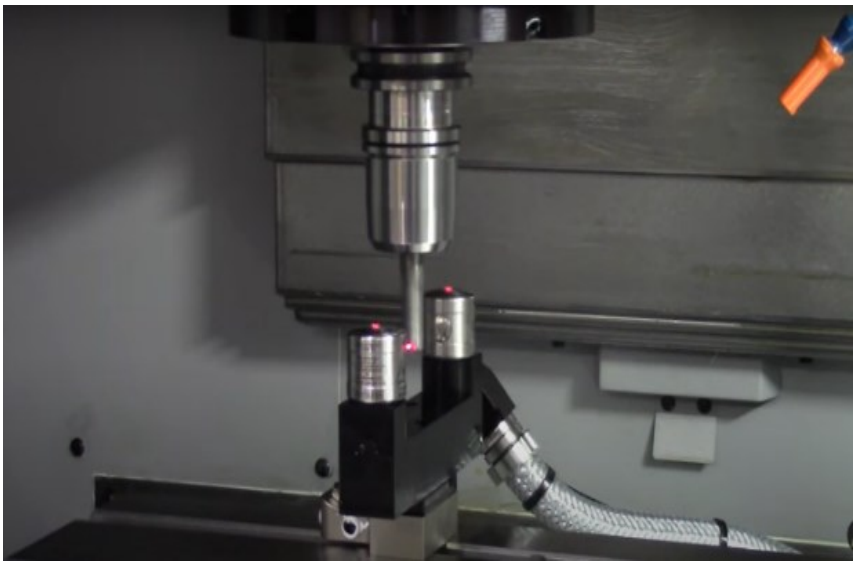

**Figure 1.1 The length of a tool is measured with a laser tool setter.**

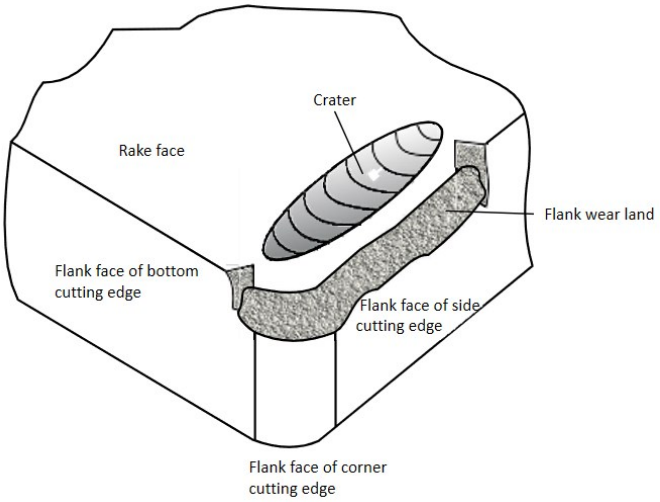


**Figure 1.2 Flank wear occurs on the insert.**

The OMM technology can directly measure tool radius and length and has applications with tool setters in the industry. Unfortunately, it cannot measure the flank wear for the TCM or predict the lifetime of cutting tools in machining. No practical on-machine technique is available for measuring or predicting flank wear. But there can be a geometric relationship between the reduction of tool size and the width of the flank wear land [9]. Therefore, the flank wear can be predicted by establishing the geometric relationship after the tool size is measured with the OMM of cutting tools. It has the advantages of measuring tool size in machining and compensating for the following tool paths. At the same time, the flank wear of the cutting tool can be predicted to monitor the tool condition.

## 1.2 Literature review

Over the years, many researchers have conducted studies about tool wear. For research on flank wear prediction, Odedeyi *et al*. [10] carried out an experimental study for flank wear in end-milling AISI 316 stainless steel with coated carbide inserts. The experimental results showed that

the flank wear decreases with increasing cutting speed. The flank wear was the major and predominant failure mode affecting the tool life. Wang *et al*. [11] proposed the Gaussian mixture regression model (GMR) to realize robust tool wear prediction. The relationship between the tool wear value and the features was built as the characteristic of the GMR model, providing an incredible accuracy in predicting tool wear. Iqbal *et al*. [12] used fuzzy-rules-based strategies for flank wear estimation in the hard milling process. Experiments were performed to obtain data for developing two fuzzy expert systems. The online system showed 67.9% more accuracy than the offline system in predicting flank wear. Lu *et al*. [13] proposed a flank wear prediction model in milling Inconel 718. The model was based on the 3D finite element simulation, and it was relatively easy to operate with a low cost. Roney *et al*. [14] predicted tool flank wear and tool failure in face milling. The spectral content of the audible acoustic emission signals can be used to predict the cumulative flank wear in real-time for an indexable carbide insert in a milling process. Kaya *et al*. [15] developed an online TCM system for milling Inconel 718 superalloy. An effective and efficient strategy based on artificial neural networks was presented to estimate tool flank wear. Singh and Rao [16] developed an analytical tool wear model for the mixed ceramic inserts during the hard turning. The model could predict the flank wear using the cutting parameters and tool geometry. Sreeraj *et al*. [17] researched the determination of the variation in acoustic signal characteristics with tool flank wear in the conventional turning process using Fast Fourier Transformation. The work optimized the distance of the tool wear sensor position and established a relationship between flank wear and the amplitude of acoustic signals. Experimental results showed the average percentage deviation of the predicted flank wear is 9.97%.

Also, many researchers focus on cutting force, vibration, or noise sound signals to establish tool wear models. Kuram and Ozcelik [18] proposed that the wear of the cutting tool is influenced by its actual shape and material, the machine spindle run-out, the workpiece material, the cutting parameters, and the coolant. Ozel *et al*. [19] investigated the influence of cutting parameters on the tool flank wear and surface roughness in the finish turning of hard steel. In this work, multiple linear regression models and neural network models based on cutting parameters were developed for predicting surface roughness and tool flank wear. Choudhury and Rath [20] indicated tool wear regarding cutting parameters and cutting force, and the maximum deviation between the

experimental and the predicted tool wears is 8%. Compared to the model established earlier, the proposed model predicted tool wear with higher accuracy. In the work of Sarhan *et al*. [21], the relationship between cutting force harmonics and tool wear was constructed for cutting force simulation. The tool wear was measured offline, which constructed an interrelationship with cutting force harmonics. Thus, a strategy of tool wear monitoring was proposed. Sick [22] put forward a hybrid approach to monitoring tool wear in turning. It integrates a physical model of cutting force in terms of cutting parameters with a neural network model of tool wear in terms of cutting force. Zhang *et al*. [23] studied tool wear and cutting forces in end-milling Inconel 718 with coated cutting tools in dry cutting and MQCL cutting with biodegradable vegetable oil. The relationship between tool wear and the cutting force variations under different cutting conditions is also explored. Jozic *et al*. [24] conducted experiments to establish the relationship of flank wear with cutting force, cutting speed, feed per tooth, and radial depth of cut. Using the functional data analysis method, a linear regression model is developed for tool wear. The efficiency and flexibility of the developed model have been verified by comparing it with the separate experimental data set. Mohanraj and Shanmugam [25] used an integrated kurtosis-based algorithm for Z-filter (I-Kaz) analysis. The vibration signals in the milling of Inconel 625 were examined to monitor tool wear. The results revealed that the I-Kaz coefficient is correlated with flank wear. Hosseini Aghdam and Cigeroglu [26] considered the problem of tool wear estimation using vibration signals via the non-stationary functional series time-dependent autoregressive moving average (FSTARMA) model. In this work, tool wear and vibrations are correlated by the autoregressive distance and the damping ratios of tool-holder bending modes.

There are also researches combining the tool wear model and the tool life prediction. Li [27] reviewed many articles on theoretical analysis and numerical simulation of tool wear. This paper introduces the hidden Markov models to estimate tool wear in cutting and the finite element methods to predict the tool wear evolution and the tool life in orthogonal cutting. Zhou *et al*. [28] predicted a tool's remaining life under variant machining conditions. Their work unifies the machining conditions and extracts tool wear information from the cutting-force signals. Kwon and Fischer [29] developed the tool wear index and the tool life model to analyze the wear surface area and the tool material loss using micro-optics, image processing, and analysis algorithms. Adesta *et*

*al*. [30] established a new model for estimating tool life during high-speed hard turning based on the relationship between the flank wear progress and time. Karandikar [31] proposed a machine learning classification method for modeling tool life using tool wear data. It offers a powerful and practical approach for modeling tool life in machining in an industrial setting. Lajis *et al*. [32] designed a tool life model in end milling of hardened steel AISI D2. The independent variables selected in the model included the cutting speed, feed, and depth of cut. Design-Expert 6.0 software was used to develop the tool life equations as the predictive models. Oraby and Hayhurst [33] developed the non-linear regression analysis techniques for wear and tool life determination in terms of the variation of a ratio of force components acting at the tooltip. A model which related an average measure of wear to the cutting parameters, time, and thrust force ratio was developed. A further model was also established, which combines the tool life and the cutting parameters as well as final thrust force ratios.

## 1.3 On-machine measurement with a laser tool setter

On-machine measurement techniques are prevalent in modern manufacturing. In terms of application devices, on-machine measurement techniques consist of two major categories: measure parts with touch probes and measure cutters with tool setters. An advanced on-machine tool measurement system with a laser tool setter is developed to mainly study the measurement of cutting tools. The system has three parts: a laser tool setter device, an interface unit, and a CNC control [34]. The laser tool setter is equipped with a laser transmitter and an optical receiver (see Fig. 1.3). It can transform the physical movement into a digital signal. The interface unit can process signals from the tool setter and communicate these to the CNC machine controller (see Fig. 1.4). The CNC machine is the receiver of the signals (see Fig. 1.5). It can also provide a programming environment for the tool setting software of measuring cutting tools. The main measurement procedure is that the operator runs the tool setting software after setting measurement tasks and programming. The machine tool is controlled to perform measuring and activate the tool setter. The triggered signal is processed to the interface unit during the interaction between the cutting tool and the tool setter. Then, a solid-state relay signal is output to the machine tool. The

tool setting software will calculate the tool radius and length and updates the tool offsets. The tool path is automatically compensated with new tool offsets in the following machining.

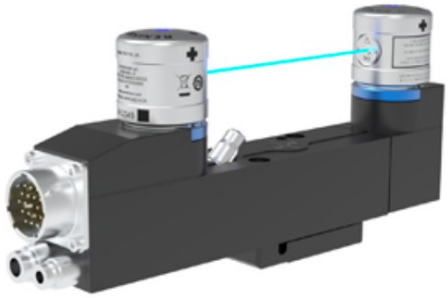

**Figure 1.3 The laser tool setter processes triggered signals.**


**Figure 1.4 The interface unit converts signals.**

**Figure 1.5 The CNC machine is the receiver of signals.**

Applying on-machine tool measurement with the laser tool setter improves the machining accuracy as opposed to human error induced by manual offsets. In addition, it has advantages compared to an offline tool setting. The cutting tool is measured while rotating, which eliminates errors caused by the spindle run-out, the holder, and the cutting tool itself. The consistency of measurement is also guaranteed. It simplifies the measuring processes because no manual touch-off is required, which is more convenient and secure for operators.

## 1.4 Tool condition monitoring

In machining, tool wear occurs in any cutting process. With the gradual increase of tool wear, the tool's cutting performance becomes worse, which finally leads to tool failure. It results in reduced productivity and economic losses. The reliable tool condition monitoring is essential for pretending this problem and optimizing the utilization of the tool life [35]. Nowadays, an experienced machinist can pay close attention to the performance of the cutting tool and monitor the tool condition manually. They usually focus on the surface quality of the workpiece, the chip condition, noise, and vibration of the cutting tool. This cannot accurately monitor the wear of the tool, and it will consume a lot of human resources and time costs in the mass production of processing. Also, the recent trend of intelligent manufacturing with modern unsupervised CNC

machines has changed the machining environment significantly. The operators are not always available to keep an eye on machining conditions and make tool-changing decisions timely. Thus, the technology of tool condition monitoring has become a great demand.

Methods of tool condition monitoring are mainly applied by tool wear sensing, which helps monitor the progression of cutting tool wear and the optimum use of cutting tools. A sensor, a signal regulator, and a monitor are included in the TCM system [36]. Sensors are placed close to the monitored target and execute the signal regulator to obtain useful information and convert the signal to a monitor. Signals are displayed and analyzed by a monitor device. Figure 1.6 shows a schematic of the tool condition monitoring system. First, the data of signals from the sensor are collected. Second, the data are processed, and valuable features are extracted. Then, the tool wear is classified or estimated by identifying patterns, fuzzy methods, or regression analysis. At last, techniques are developed to reflect tool wear conditions and make decisions to change tools.

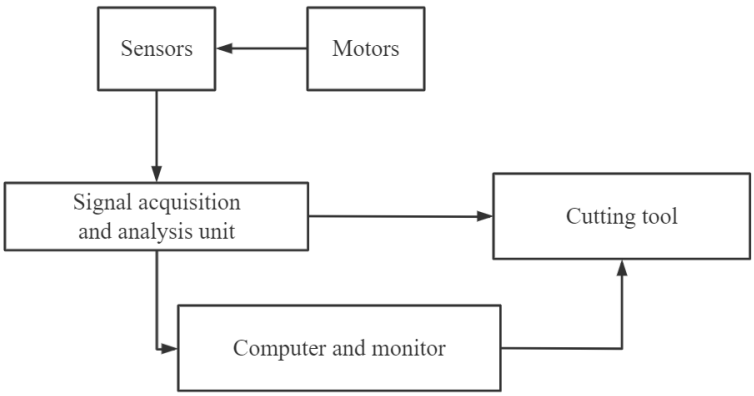


**Figure 1.6 The TCM system consists of sensors, signal regulators, and monitors.**

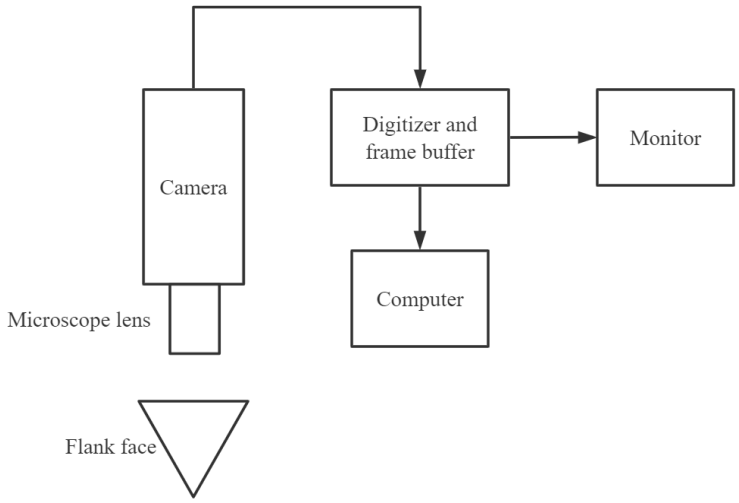


**Figure 1.7 Optical equipment is used for tool wear sensing.**

Tool condition monitoring is classified into two main groups: direct methods and indirect methods. Direct methods are based on the vision system. Tool wear is measured and displayed using optical or radioactive techniques. Figure 1.7 shows a tool wear sensing system with the camera and microscopic lens. The actual geometric changes arising from the tool wear are captured directly. However, it is less advantageous because the cutting area is largely inaccessible, and there is continuous contact between the cutting tool and the workpiece. In addition, it's more difficult to apply this method in practice due to the coolant on the cutting tool. Thus, there comes up with the indirect methods. Tool wear is not detected directly but achieved from the measurable parameters through sensors. Many studies use the indirect method to monitor tool wear and predict tool life, which is reviewed in the previous section. Typical parameters for reflecting tool wear include cutting forces, vibrations, temperature, surface roughness, torque, etc. The method measured those parameters correlated to actual wear and effectively monitor tool conditions with computer aid. But on the other hand, it needs plenty of experiments and mathematical skills in data analysis to establish the relationship between the parameters and tool wear.

The most predominant wear mechanism is the flank wear in tool condition monitoring. Flank wear occurs on the flank face of the cutting tool, and the width of the flank wear land is commonly used as the criteria for judging whether cutting tools fail. For example, flank wear usually occurs on the insert. When the insert is cutting a workpiece, the insert's cutting edge removes the workpiece material. At the same time, its flank face rubs the surface just machined, causing flank wear and generating an irregular land, which is shown in Figure 1.8. As the flank wear increases, the width of flank wear land gets larger, increasing cutting force and reducing the machined surface finish. Eventually, other types of tool wear occur; when chipping is generated on the side cutting edge, the insert is invalid and should be changed immediately. The insert flank wear removes a piece of the original cutting edge and generates a new cutting edge inside the rake face. Usually, the flank wear is irregular, so the width of the flank wear land is not constant. A professional way to define the width is to project the flank wear land on a vertical plane (normal to the rake face), and the vertical distance $V_B$ of the land is the flank wear width (see Fig. 1.9). The maximum width represents the flank wear. When the maximum width reaches the threshold, the tool fails. Hence to detect the insert's failure for the TCM, the maximum width should be monitored, and the insert should be replaced before it fails.

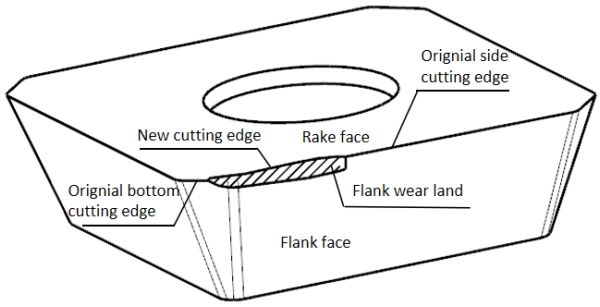


**Figure 1.8 The flank wear land is generated on the insert.**

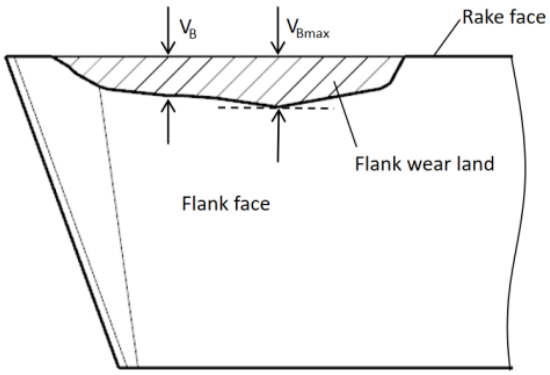


**Figure 1.9 The vertical distance of the flank wear land is the flank wear width.**

## 1.5 Research objectives

This thesis proposes a practical and direct approach for OMM-TCM fusion based on the laser tool setter. The main objective is to measure tool size to compensate for tool paths in the following machining and predict the flank wear for tool condition monitoring. The work focuses on two end-mills: the indexable face mill and the fillet end-mill. It can be concluded in the following aspects:

- The geometric models of the end-mills are built accurately.
- The geometric relationship between tool radius and the width of the flank wear land is established.
- An experimental method of recognizing the flank wear pattern is adopted to determine measurement locations according to the geometric relationship.

The end-mill is measured for radius and lengths with a laser tool setter at the determined locations. The tool radius and length in the CNC controller are updated with the newly measured

data. In the following machining, tool paths will be compensated. When a tool radius is measured at a location, the width of the corresponding flank wear land is calculated using the geometric relationship. The land widths at all locations are calculated and compared to the threshold for tool condition monitoring. If a land width exceeds the threshold, the end-mill is invalid and should be replaced.

## 1.6 Outline

The thesis is organized as follows. In Chapter 2, a geometric model of the fillet end-mill is built based on modeling principles. Chapter 3 establishes a model of the indexable face mill, and the flank wear land of the insert is studied. In Chapter 4, the relationship between tool radius and the width of the flank wear land is established for the indexable face mill. In chapter 5, experiments are conducted to determine measurement locations of an indexable face mill, and the proposed approach in this thesis is verified. At last, Chapter 6 gives the conclusions.

# Chapter 2 Geometric Model of a Fillet End-mill

## 2.1 Modeling principles

The first research end-mill in the thesis is the fillet end-mill. A fillet end-mill is also called a corner rounding end-mill, which is a type of end-mills with a rounded corner at the bottom of the tool body (see Fig. 2.1). Compared with ordinary end-mills, it can improve machining surface quality and tool life. To study its flank wear model, the theoretical model of the fillet end-mill must be built accurately. There are many mature methods to model an ordinary end-mill without the fillet. However, there are no practical standards or procedures to model the flank face on the fillet for the fillet end-mill. The cutting edge on the fillet often cuts the workpiece, and the fillet flank face is in contact with the workpiece surface, leading to flank wear. Therefore, the key to accurately modeling the fillet end-mill is to model the fillet flank face.


**Figure 2.1 The end-mill has a fillet.**

In this section, a practical method is proposed to model the flank face on the fillet using CAD software. The modeling principles are determined by practical experience in manufacturing fillet end-mills. The principles can be summed up as follows.

1. The flank face on the fillet is smoothly connected to the flank face of the side cutting edge and the flank face of the bottom cutting edge.

2. The relief angle of the flank face on the fillet is as close as possible to the design relief angle.

According to the principles, an original end-mill is modeled based on the cylinder tool body with a fillet. The fillet cutting edge has no flank face. Figure 2.2 shows the partial view of the fillet. $\mathbf{SS}_1$ is the side cutting edge, **SH** is the fillet cutting edge, and $\mathbf{HH}_1$ is the bottom cutting edge. Meanwhile, $\mathbf{E}_1\mathbf{E}_2$ and $\mathbf{F}_1\mathbf{F}_2$ are the bottom boundaries of the bottom flank face and the side flank face, respectively. The yellow surface in Fig. 2.2 represents the fillet surface, but it's not the flank face on the fillet. Instead, it's a part of the cylinder tool body. Thus, a surface should be modeled as the flank face on the fillet that complies with the above modeling principles.

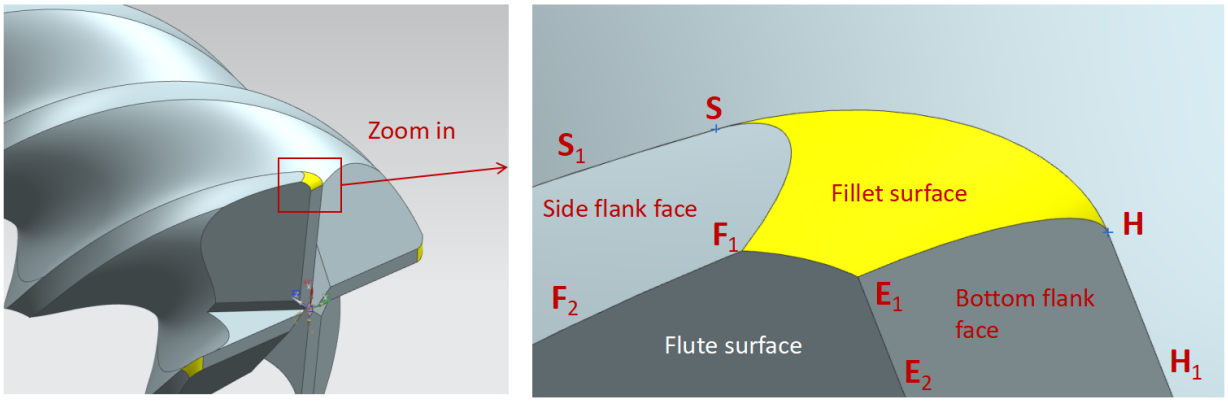


**Figure 2.2 The fillet of the end-mill is zoomed in.**

## 2.2 Continuity of the flank face

The whole flank face of a fillet end-mill should be a smooth surface. So, the fillet flank face to be modeled should be smoothly connected to the flank face of the side cutting edge and the flank face of the bottom cutting edge. In other words, there should be G1 continuity between flank faces. It can be divided into three details to ensure continuity. (1) The three surfaces are G0 connected

and have no gaps. (2) The upper boundary of the three faces is G1 continuous, and the lower boundary of the three faces is also G1 continuous. (3) A ruled surface is formed based on the boundaries as the flank face on the fillet.

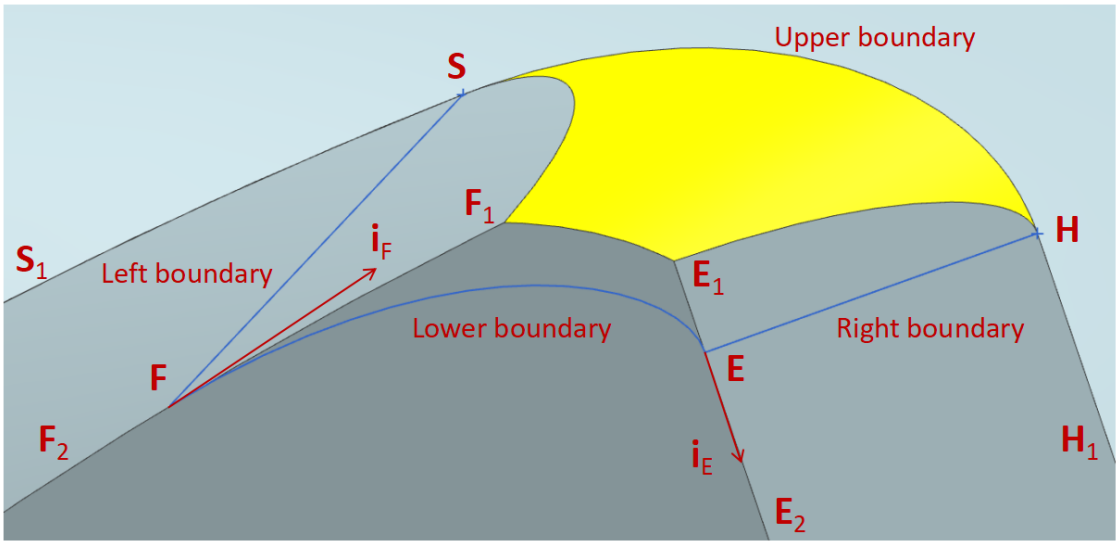


**Figure 2.3 Four boundary lines of the fillet flank face are formed.**

Figure 2.3 shows the boundary lines of the fillet flank face to be modeled. The upper boundary of the flank face is the cutting edge, and the whole cutting edge of the end-mill is smooth. Thus, the upper boundary **SH** of the fillet flank face is G1 continuous with the upper boundary $\mathbf{SS}_1$ of the side flank face and the upper boundary $\mathbf{HH}_1$ of the bottom flank face. The straight line **SF** is the intersection of the orthogonal plane at point **S** and the side flank face, which is also the left boundary of the fillet flank face. On the other side, the straight line **HE** is on the bottom flank face plane as the right boundary of the fillet flank face. The endpoints **F** and **E** of the lower boundary are determined.

Meanwhile, the unit tangent vector $\mathbf{i}_F$ of the curve $\mathbf{F}_1\mathbf{F}_2$ at point **F** and the unit tangent vector $\mathbf{i}_E$ of the curve $\mathbf{E}_1\mathbf{E}_2$ at point **E** can also be obtained. So, a Hermite curve **FE** can be formed as the bottom boundary of the fillet flank face. The unit tangent vectors of the Hermite curve **FE** at points

**F** and **E** are vectors $\mathbf{i}_F$ and $\mathbf{i}_E$, respectively, which guarantees the G1 continuity between the lower boundaries.

A ruled surface **S - H - E - F** can be modeled as the fillet flank face after the boundaries are determined, as shown in Fig. 2.4. The group of straight lines used to form the ruled surface is also shown. In the manufacture of end-mills, the flank face is ground by the grinding wheel. The positions of those straight lines can be extracted as the reference for the positioning of the grinding wheel. It makes the fillet end-mill model more significant in practice.

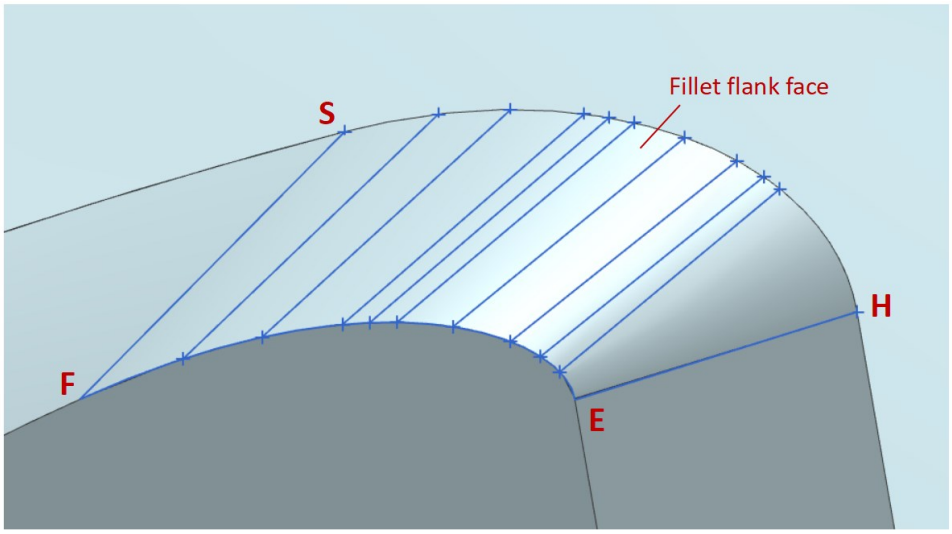


**Figure 2.4 A ruled surface is modeled as the fillet flank face.**

## 2.3 Relief angle requirement

The design relief angle determines the position of the lower boundary of the flank face on the fillet. However, the relief angle at every height of the fillet flank face cannot be completely equal to the design relief angle due to the surface's complexity and the continuity between flank faces. According to the machining experience, (1) the position at the height of half the fillet radius is where the maximum flank wear usually occurs, and (2) the position close to the bottom edge is

often participated in cutting workpiece in practical. The relief angle at these positions should be equal to the design relief angle. Thus, the Hermite curve as the lower boundary of the fillet flank face can be optimized based on the design relief angle at these positions.

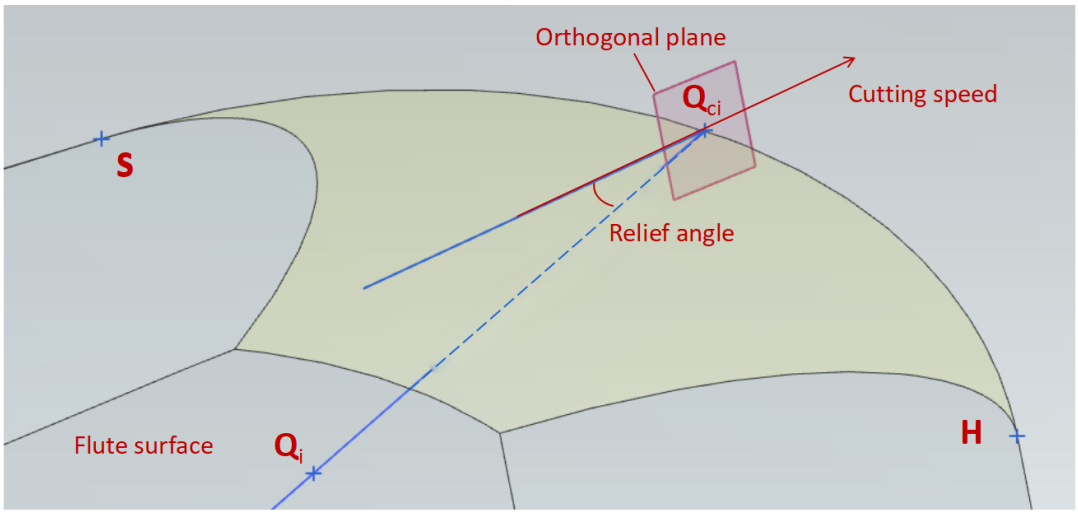


**Figure 2.5 $Q_i$ is a reference point of the Hermite curve's position.**

One of the reference positions of the Hermite curve is determined as shown in Fig. 2.5. Point $\mathbf{Q}_{ci}$ is on the cutting edge **SH**, and the cutting speed direction at the height of point $\mathbf{Q}_{ci}$ is the tangent of **SH** on the orthogonal plane. According to the geometry, the angle between the flank face and the direction of cutting speed of the end-mill is the relief angle. Thus, a straight line is $\mathbf{Q}_{ci}\mathbf{Q}_i$ formed on the orthogonal plane with the relief angle, intersecting with the flute surface at point $\mathbf{Q}_i$, a reference point of the Hermite curve's position. On the fillet cutting edge, several reference points of $\mathbf{Q}_{ci}$ are selected (see Fig. 2.6). Point $\mathbf{Q}_{cim}$ is assumed as the position on the cutting edge at the height of half the fillet radius. According to the principles, the reference points of $\mathbf{Q}_{ci}$ are mainly near point $\mathbf{Q}_{cim}$ and close to endpoint **H** on the cutting edge. Following the procedure above, there is a point set of $\mathbf{Q}_i$ on the flute surface as the reference points for positioning the Hermite curve, as shown in Fig. 2.7. The coordinates of these points can be obtained directly.

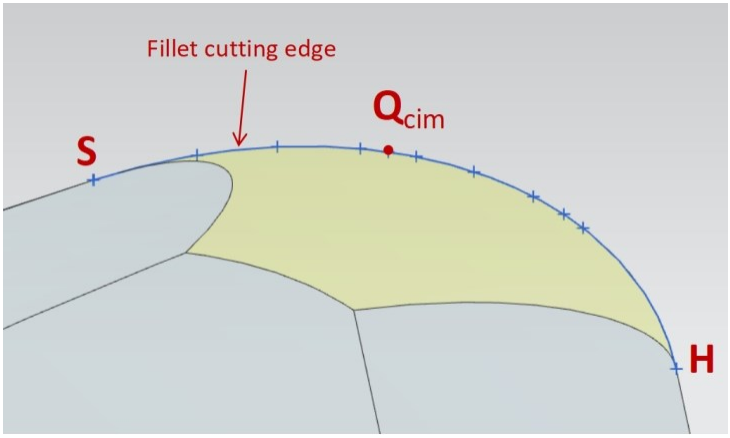


**Figure 2.6 Reference points are selected on the fillet cutting edge.**

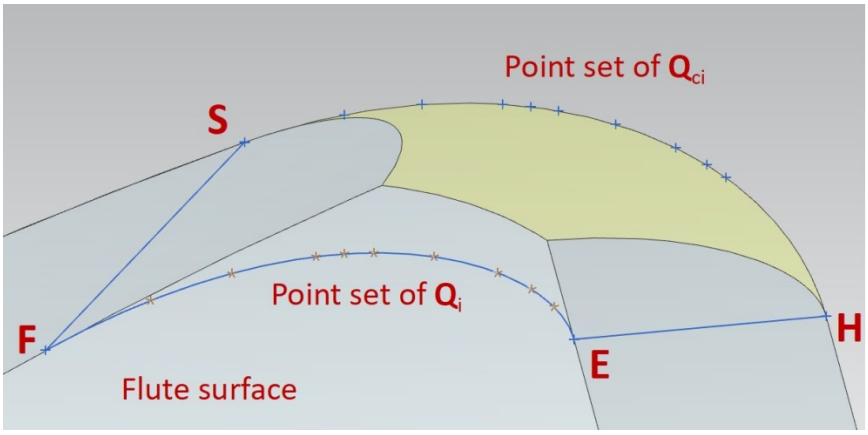


**Figure 2.7 Reference points of $Q_i$ are formed on the flute surface.**

To ensure the relief angle of the fillet flank face at these points is as close as possible to the design relief angle, the Hermite curve should be optimized to close to the position reference points of $\mathbf{Q}_i$. The optimization process of the Hermite curve is as follows. First, the parametric equation of the curve is

$$\mathrm{P}(u)=\begin{bmatrix} x(u) & y(u) & z(u) \end{bmatrix}=a_0+a_1\cdot u+a_2\cdot u^2+a_3\cdot u^3. \tag{2.1}$$

where $u$ is the parameter in the interval of [0, 1], parameters $a_0$, $a_1$, $a_2$, and $a_3$ in the equation are shown as follows.

$$a_0 = \mathbf{F} = \begin{bmatrix} x_{\mathrm{F}} & y_{\mathrm{F}} & z_{\mathrm{F}} \end{bmatrix}, \tag{2.2}$$

$$a_1 = \mathbf{F}' = \mathbf{i}_{\mathrm{F}} \cdot k_1, \tag{2.3}$$

$$a_2 = -3 \cdot \mathbf{F} + 3 \cdot \mathbf{E} - 2 \cdot \mathbf{F}' - \mathbf{E}', \tag{2.4}$$

$$a_3 = 2 \cdot \mathbf{F} - 2 \cdot \mathbf{E} + \mathbf{F}' + \mathbf{E}'. \tag{2.5}$$

**E** and **F** are the coordinates of the endpoints of the Hermite curve, **E**' and **F**' are the corresponding tangent vectors.

$$\mathbf{F} = \begin{bmatrix} x_{\mathrm{F}} & y_{\mathrm{F}} & z_{\mathrm{F}} \end{bmatrix}, \tag{2.6}$$

$$\mathbf{F}' = \mathbf{i}_{\mathrm{F}} \cdot k_1 = \begin{bmatrix} x_{\mathrm{F}}' \cdot k_1 & y_{\mathrm{F}}' \cdot k_1 & z_{\mathrm{F}}' \cdot k_1 \end{bmatrix}', \tag{2.7}$$

$$\mathbf{E} = \begin{bmatrix} x_{\mathrm{E}} & y_{\mathrm{E}} & z_{\mathrm{E}} \end{bmatrix}, \tag{2.8}$$

$$\mathbf{E}' = \mathbf{i}_{\mathrm{E}} \cdot k_2 = \begin{bmatrix} x_{\mathrm{E}}' \cdot k_2 & y_{\mathrm{E}}' \cdot k_2 & z_{\mathrm{E}}' \cdot k_2 \end{bmatrix}'. \tag{2.9}$$

In the above equations, $k_1$ and $k_2$ are the vectors' modulus, which are the unknown parameters that need to be optimized so that the curve is close to the reference points. The equation (2.1) is transformed into the following expressions.

$$\begin{cases} x(u) = x_{\mathrm{F}} + k_1 \cdot x_{\mathrm{F}}' \cdot u + \left(3 \cdot x_{\mathrm{E}} - 3 \cdot x_{\mathrm{F}} - 2 \cdot k_1 \cdot x_{\mathrm{F}}' - k_2 \cdot x_{\mathrm{E}}'\right) \cdot u^2 + \left(2 \cdot x_{\mathrm{E}} - 2 \cdot x_{\mathrm{F}} + k_1 \cdot x_{\mathrm{F}}' + k_2 \cdot x_{\mathrm{E}}'\right) \cdot u^3 \\ y(u) = y_{\mathrm{F}} + k_1 \cdot y_{\mathrm{F}}' \cdot u + \left(3 \cdot y_{\mathrm{E}} - 3 \cdot y_{\mathrm{F}} - 2 \cdot k_1 \cdot y_{\mathrm{F}}' - k_2 \cdot y_{\mathrm{E}}'\right) \cdot u^2 + \left(2 \cdot y_{\mathrm{E}} - 2 \cdot y_{\mathrm{F}} + k_1 \cdot y_{\mathrm{F}}' + k_2 \cdot y_{\mathrm{E}}'\right) \cdot u^3 \\ z(u) = z_{\mathrm{F}} + k_1 \cdot z_{\mathrm{F}}' \cdot u + \left(3 \cdot z_{\mathrm{E}} - 3 \cdot z_{\mathrm{F}} - 2 \cdot k_1 \cdot z_{\mathrm{F}}' - k_2 \cdot z_{\mathrm{E}}'\right) \cdot u^2 + \left(2 \cdot z_{\mathrm{E}} - 2 \cdot z_{\mathrm{F}} + k_1 \cdot z_{\mathrm{F}}' + k_2 \cdot z_{\mathrm{E}}'\right) \cdot u^3 \end{cases} \tag{2.10}$$

For a specific reference point $\mathbf{Q}_{\mathrm{i}}$, the distance between the Hermite curve and the reference point is

$$\mathrm{D}_{\mathrm{i}}(u) = \left[x(u) - x_{\mathrm{Qi}}\right]^2 + \left[y(u) - y_{\mathrm{Qi}}\right]^2 + \left[z(u) - z_{\mathrm{Qi}}\right]^2. \tag{2.11}$$

In this model, the design relief angle is set to be 15°, and the fillet radius is 1 mm. There are 9 points selected as the position reference. Also, the endpoints' coordinates and their unit tangent vectors are obtained.

$$\mathbf{F} = \begin{bmatrix} -9.394 & 2.54 & 1 \end{bmatrix}, \tag{2.12}$$

$$\mathbf{F}' = \mathbf{i}_{\mathrm{F}} \cdot k = \left[-0.247 \cdot k_1 \quad -0.813 \cdot k_1 \quad -0.528 \cdot k_1\right]', \tag{2.13}$$

$$\mathbf{E} = \left[-9.061 \quad 1.155 \quad 0.101\right], \tag{2.14}$$

$$\mathbf{E}' = \mathbf{i}_{\mathrm{E}} \cdot k_2 = \left[k_2 \quad 0 \quad 0\right]'. \tag{2.15}$$

The coordinates and parameters of these points are listed in Table 2.1. It's noticed that parameter $u$ is determined by the length of curve $\mathbf{FQ}_i$ divided by the length of the whole curve **FE**.

**Table 2.1 The coordinates and parameters of point $\mathbf{Q}_i$.**

| $i$ | Coordinates of point $\mathbf{Q}_i$ | | | $u$ |
|---|---|---|---|---|
| | $x_i$ | $y_i$ | $z_i$ | |
| 1 | -9.46 | 2.23 | 0.8 | 0.088 |
| 2 | -9.48 | 2 | 0.65 | 0.2 |
| 3 | -9.46 | 1.77 | 0.5 | 0.32 |
| 4 | -9.45 | 1.69 | 0.45 | 0.4 |
| 5 | -9.43 | 1.6 | 0.4 | 0.49 |
| 6 | -9.37 | 1.47 | 0.3 | 0.6 |
| 7 | -9.28 | 1.31 | 0.2 | 0.7 |
| 8 | -9.22 | 1.23 | 0.15 | 0.8 |
| 9 | -9.18 | 1.18 | 0.12 | 0.9 |

After substituting the above data, equation (2.11) contains only two unknown parameters, $k_1$ and $k_2$. Then, sum the distances from positions on the Hermite curve to the reference points; the objective function to be optimized is

$$\mathrm{D_s}(u)=\sum_{\mathrm{i}=1}^{9}\mathrm{D_i}(u). \tag{2.16}$$

An optimization model is built in MATLAB by combining the equations from (2.10) to (2.16) and substituting the data in Table 2.1. The two unknown parameters, $k_1$ and $k_2$, can be solved as well as the minimum sum of distance. The solution is given below.

$$\begin{cases}\left[k_1 \quad k_2\right]=\left[3.22 \quad 0.754\right] \\ \min\left[\mathrm{D_s}(u)\right]=0.039\end{cases}. \tag{2.17}$$

The parametric equation of the Hermite curve as the lower boundary of the fillet flank face is denoted as

$$\mathrm{P}(u)=\begin{bmatrix}x(u)\\ y(u)\\ z(u)\end{bmatrix}'=\begin{bmatrix}-0.708\cdot u^3+1.837\cdot u^2-0.795\cdot u-9.394\\ 0.153\cdot u^3+1.079\cdot u^2-2.617\cdot u+2.54\\ 0.0987\cdot u^3+0.702\cdot u^2-1.699\cdot u+1\end{bmatrix}'. \tag{2.18}$$

## 2.4 Verification

The flank face on the fillet is modeled by a ruled surface after determining its boundaries, and it's also optimized by the Hermite curve in the previous sections. Based on the modeling principles, the continuity between flank faces and the relief angle of the modeled flank face on the fillet should be verified. Figure 2.8 gives the G0 and G1 continuity of the fillet flank face with the side flank face and the bottom flank face. The G0 value represents the distance between two surfaces, while the G1 value represents the angle between the generatrices of the two surfaces on

the intersection line. The G0 value of both approaches to zero, which shows there is no gap between the surfaces. Due to the calculation error of the curve parametric equation, the G1 value of the fillet flank face and the side flank face is 0.0154 degrees, and the G1 value of the fillet flank face and the bottom flank face is 0.0022 degrees. It also demonstrates good G1 continuity between flank faces.

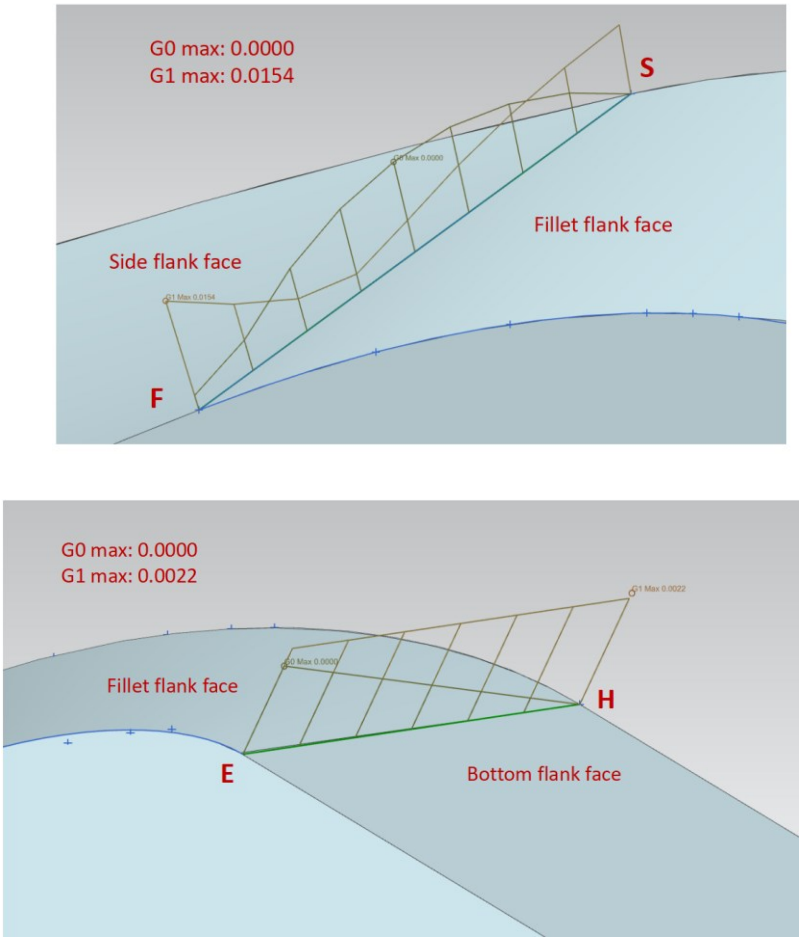


**Figure 2.8 The modeled flank faces show good continuity.**

For the requirement of the design relief angle, several positions on the fillet cutting edge are selected to measure their relief angles and verify that they are nearly the same as the design relief angles of 15 degrees. The selected positions are still (1) near the height of 0.5 mm, which is half the fillet radius, and (2) close to the bottom cutting edge. The result is shown in Table 2.2.

**Table 2.2 The relief angle of the modeled fillet flank face.**

| Heights (mm) | Relief angles (°) | Error |
|---|---|---|
| 0.1 | 15.9 | 6% |
| 0.15 | 14.97 | 0.2% |
| 0.2 | 14.4 | 4% |
| 0.3 | 14.2 | 5.3% |
| 0.45 | 14.44 | 3.7% |
| 0.5 | 14.54 | 3% |
| 0.55 | 14.63 | 2.4% |
| 0.8 | 14.99 | 0.067% |

The results show the difference between the model's relief angle and the designed relief angle of 15 degrees is within 1 degree at different heights. The maximum error of 6% occurs at the height of 0.1 mm. The main reason for the error is that it is difficult to guarantee the relief angle at the position near the junction of the surfaces. The smoothness between the flank faces is the primary modeling principle as a prerequisite. Otherwise, the model is meaningless in practice. In addition, The number of positional reference points is limited. As the lower boundary, the Hermite curve is optimized close to the position reference points rather than through them.

In this section, a fillet end-mill model is established. The flank face of the end-mill shows a good smoothness, and meanwhile, its relief angle is close to the required value.

# Chapter 3 Geometric Model of an Indexable Face Mill

## 3.1 Construction of the indexable face mill model

The other object end-mill in this thesis is the indexable face mill, which is also called the insert end-mill. A group of inserts is clamped into the tool body seats (see Fig. 3.1). If an insert's cutting edge wears out, it is unclamped and re-indexed to a fresh cutting edge, or it is replaced with a new insert. So, the indexable face mill is a cost-effective tool and widely used in machining.

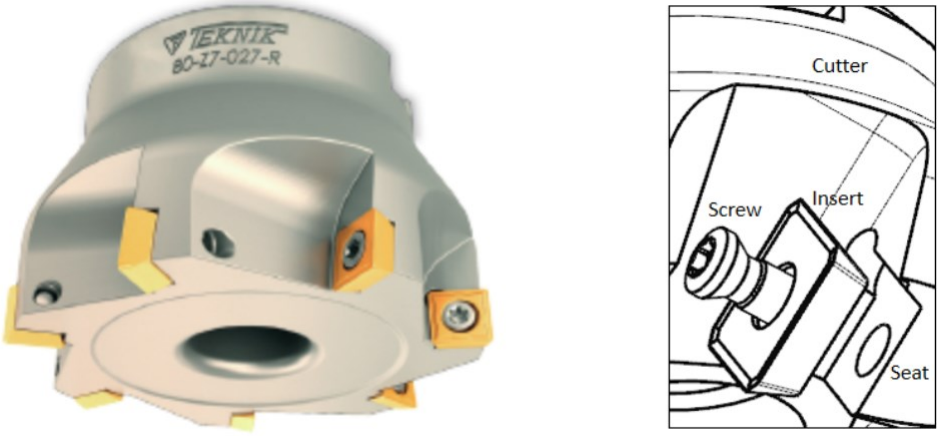


**Figure 2.9 Inserts are clamped on the indexable face mill.**

Different types of inserts have different geometries, and the inserts are clamped on the cutter with spatial angles. To build a model of the indexable face mill, the first is to model the insert accurately (see Fig. 3.2). A group of cutting edges cut the workpiece in machining: the side cutting edge, the corner cutting edge, and the bottom cutting edge. Figure 3.3 shows the tool nose after zooming in. The side cutting edge is connected to the bottom cutting edge with a corner radius of $r_c$. The intersection point of the side cutting edge and the bottom cutting edge is point $\mathbf{O}_i$. The distance between point $\mathbf{O}_i$ and the tool axis is defined as the theoretical tool radius of the indexable

face mill. Also, the angle between the side cutting edge and the bottom cutting edge is the entering angle *k* of the insert. After determining the inserts, the tool body is modeled with four seats, and four inserts are fixed into the seats with four screws, as shown in Fig. 3.4.

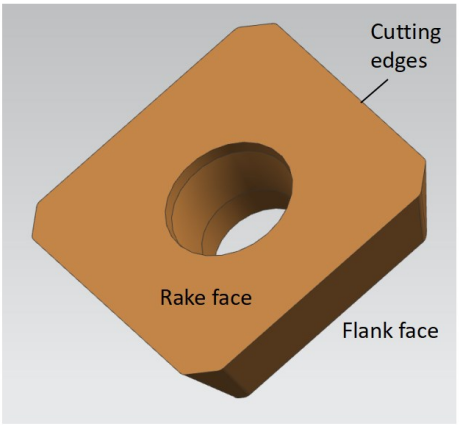


**Figure 2.10 An insert is modeled.**

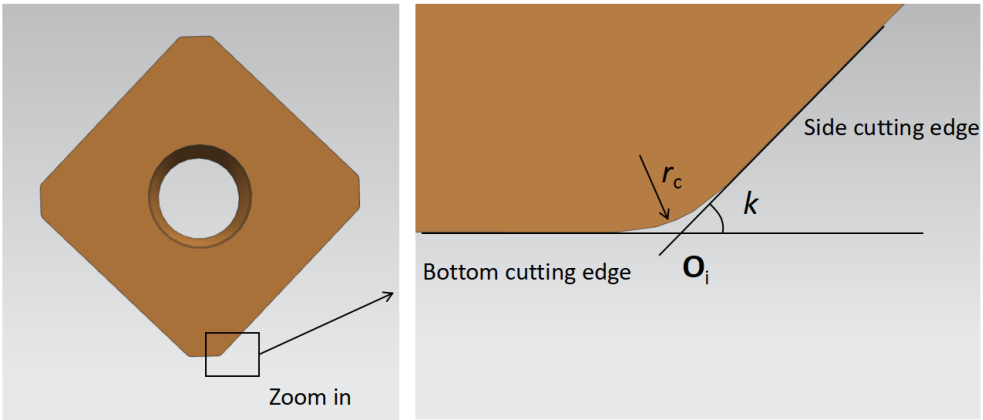


**Figure 2.11 The insert has a corner and an entering angle.**

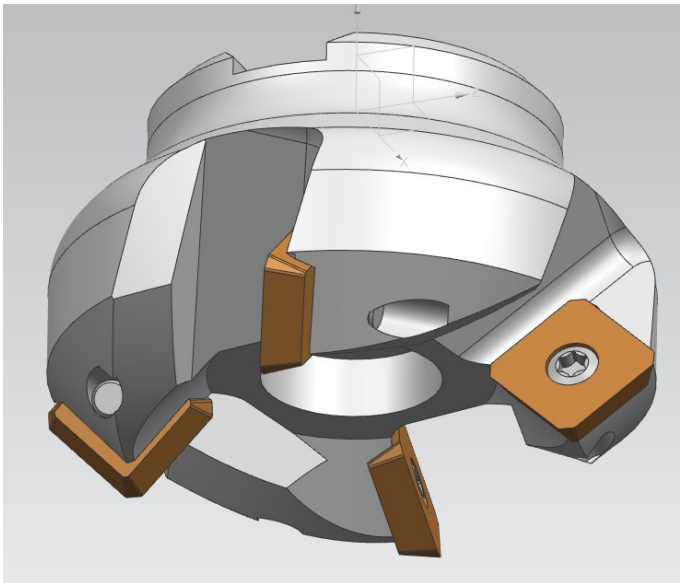

**Figure 2.12 An indexable face mill with four inserts is modeled.**

The shape of the inserts and the design of the tool body determines the geometric parameters of the indexable face mill. The most important parameter is the rake angle, which can be divided into the axial angle $\theta_a$ and the radial angle $\theta_r$. The axial angle is shown in Fig. 3.5. The rake plane is the extension of the insert's rake face, and the orthogonal plane is perpendicular to the tool axis. The two planes are not vertical due to the rake angle. Instead, there's an acute angle between the rake and orthogonal planes. Thus, the axial angle $\theta_a$ is determined by the complement of the acute angle between the rake and the orthogonal planes.

As for the radial angle $\theta_r$, it's shown in the top view of the indexable face mill in Fig. 3.6. The tool axis in the figure is represented by point $\mathbf{O}_t$, and point $\mathbf{O}_i$ represents the tool nose of the insert, which is the intersection of the side cutting edge and the bottom cutting edge. Similarly, line $\mathbf{O}_t\mathbf{O}_i$ and the bottom edge of the insert are not collinear. The radial angle $\theta_r$ is between line $\mathbf{O}_t\mathbf{O}_i$ and the bottom edge of the insert.

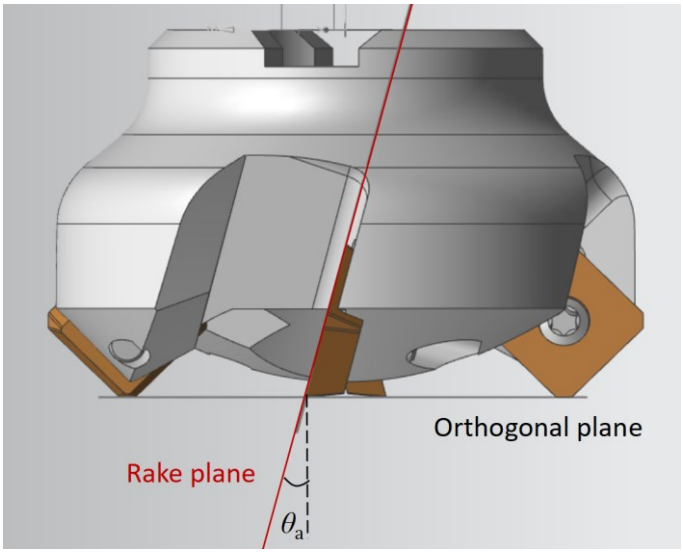


**Figure 2.13 The indexable face mill has an axial angle.**

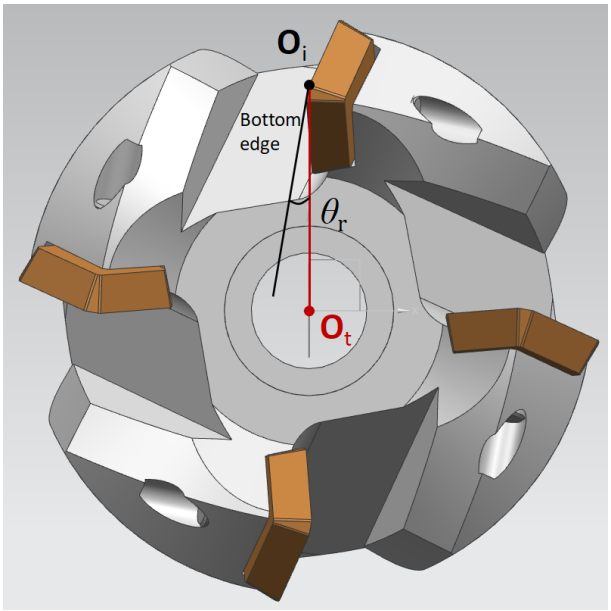


**Figure 2.14 The indexable face mill has a radial angle.**

After modeling the insert, its flank wear land can be studied. While the milling cutter is rotating, the main cutting edge is the side cutting edge and the corner cutting edge. Thus, the most severe wear usually occurs on the main cutting edge. The insert wear usually is in the form of flank

wear, and the tool condition is evaluated with the width of flank wear land. If the width exceeds the threshold, the insert life is finished, and the cutting edge should be changed.

## 3.2 Geometric model of the insert flank wear land

The geometric model of the insert's flank wear land is constructed as follows. When the cutter is rotated along its axis, one insert's original cutting edge generates a revolution surface. In machining, a piece of the original cutting edge around the cutting point wears away, and a new cutting edge is formed inside the original piece. The new cutting edge generates a revolution surface, in which the workpiece material is removed, and the machined surface is in the shape of this revolution surface. The insert material on the flank face and outside this revolution surface rubs the machined workpiece surface, eventually, the material is removed and a flank wear land is formed in the shape of the revolution surface (see Fig. 3.7).

The geometry of the flank wear land is a piece of the new revolution surface between the rake and the flank faces of the insert. Fig. 3.8 shows the larger revolution surface of the original cutting edge and the smaller one of the new cutting edge. Their radii difference is called radius reduction. Therefore, the geometric relationship between the radius reduction and the width of the flank wear land can be established.When the maximum width of the flank wear land reaches the threshold, the insert fails. There can be a geometric relationship between the flank wear land width and the radius of the new revolution surface.

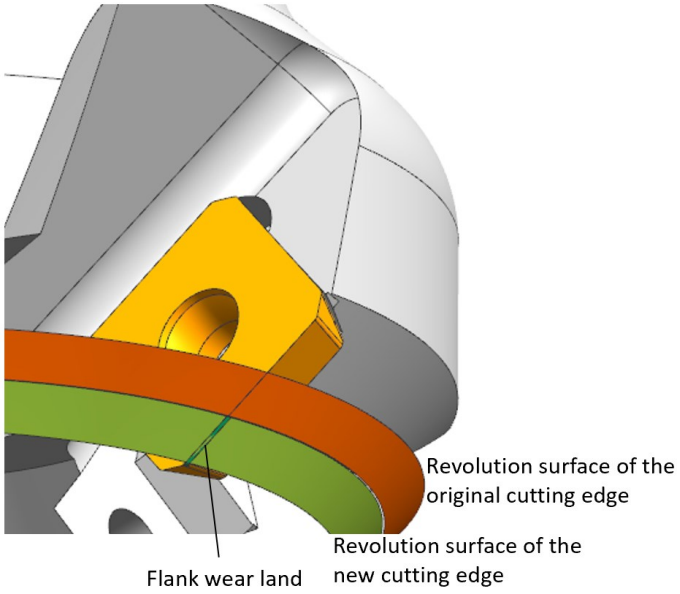


**Figure 2.15 The original revolution surface and the new revolution surface are plotted.**

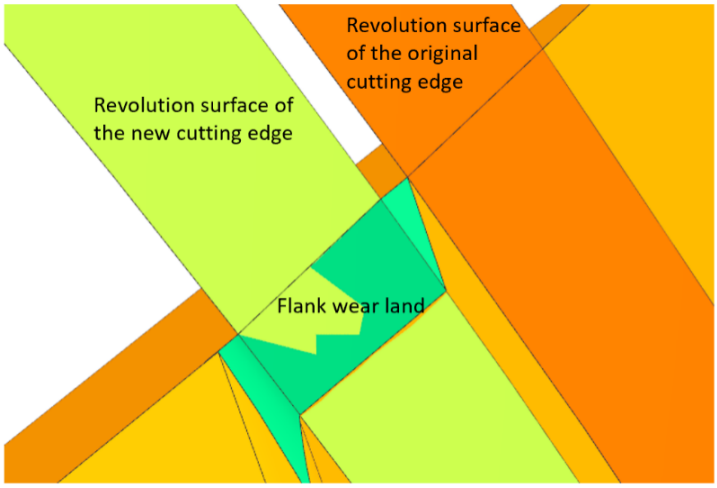


**Figure 2.16 The radius reduction is shown.**

In this chapter, the geometric model of the indexable face mill is established accurately. Also, the model of the insert's flank wear land is studied, which demonstrates a geometric theory that the flank wear can lead to a radius reduction. With OMM of cutters, the radii of the new and the worn cutters are measured in machining breaks, and their radius reduction is calculated. Equations can be derived to establish the relationship between the radius reduction and the width of flank wear land so that the tool condition monitoring can be carried out in the workpiece machining process.

# Chapter 4 Relationship Between Tool Radius and Flank Wear Land Width

## 4.1 Derivation of the transformation matrix from the insert to the tool coordinate systems

The accurate models of the fillet end-mill and the indexable face mill are built in the previous chapters. For the fillet end-mill, its flank face is a surface, which is difficult to derive its parametric equations. But for the indexable face mill, the insert's flank face is a plane. Based on the geometric model of the insert's flank wear land, the relationship between the insert radius reduction and the width of its flank wear land can be established.

For an insert of the indexable face mill, its coordinate system ($\mathbf{X}_i$ - $\mathbf{Y}_i$ - $\mathbf{Z}_i$ - $\mathbf{O}_i$) shown in Fig. 4.1 is established in the following way. Line $\mathbf{BO}_i$ is along its bottom cutting edge, and line $\mathbf{AO}_i$ is along its side cutting edge. Their intersection point is point $\mathbf{O}_i$. The origin of the insert coordinate system is at $\mathbf{O}_i$, its $\mathbf{X}_i$ axis is along vector $\mathbf{BO}_i$, its $\mathbf{Z}_i$ axis passes through $\mathbf{O}_i$ and is perpendicular to line $\mathbf{BO}_i$, and its $\mathbf{Y}_i$ axis is determined according to the right-hand rule. The entering angle $k$ is a measure from the $\mathbf{X}_i$ axis to $\mathbf{O}_i\mathbf{A}$.

The coordinate system of the indexable face mill ($\mathbf{X}_t$ - $\mathbf{Y}_t$ - $\mathbf{Z}_t$ - $\mathbf{O}_t$) is established as follows (see Fig. 4.2). When an insert is clamped into the tool body seat, a plane passing through point $\mathbf{O}_i$ and perpendicular to the tool axis intersects the tool axis at $\mathbf{O}_t$. The origin of the tool coordinate system is at $\mathbf{O}_t$, its $\mathbf{Z}_t$ axis is along the tool axis, its $\mathbf{X}_t$ axis is defined with vector $\mathbf{O}_t\mathbf{O}_i$, and its $\mathbf{Y}_t$ axis is determined according to the right-hand rule. The length of $\mathbf{O}_t\mathbf{O}_i$ is the tool radius $r$. Based on the tool design, the geometric relationship between the insert and the tool coordinate systems can be determined. In Fig. 4.2, the insert is clamped into the cutter body seat with two parameters, radial angle $\theta_r$ and axial angle $\theta_a$. The radial angle $\theta_r$ is measured from $\mathbf{X}_t$ to $\mathbf{X}_i$, and the axial angle

$\theta_a$ is measured between the $\mathbf{Z}_i$ axis and plane **PI**, which passes through the $\mathbf{O}_i\mathbf{X}_i$ axis and is perpendicular to the plane $\mathbf{X}_i\mathbf{Y}_i$.

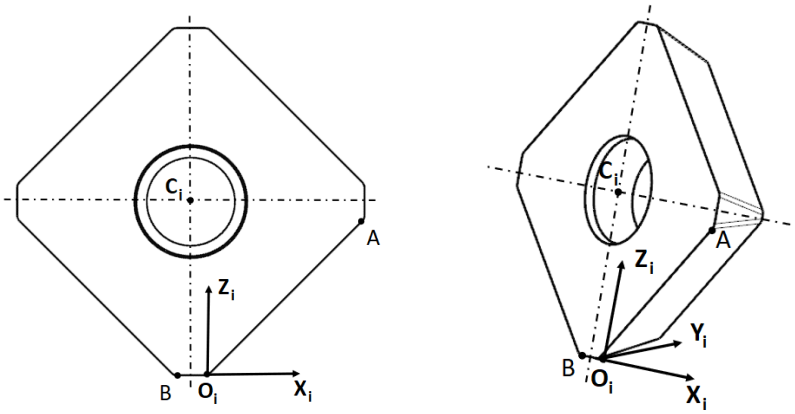


**Figure 2.17 An insert coordinate system is built up.**

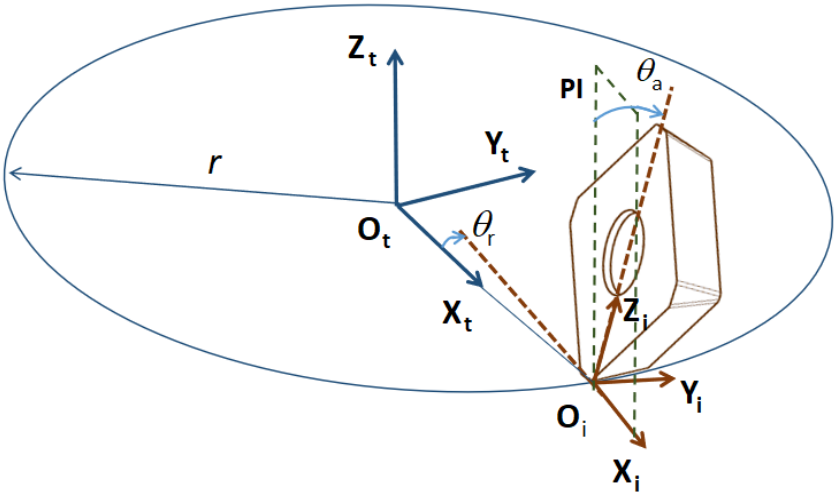


**Figure 2.18 The geometric relationship of the two coordinate systems is shown.**

According to the geometric relationship between the tool and the insert coordinate system, at first, $\mathbf{X}_i$ - $\mathbf{Y}_i$ - $\mathbf{Z}_i$ - $\mathbf{O}_i$ is rotated about the $\mathbf{X}_i$ axis by axial angle $\theta_a$. The rotation matrix is

$$\mathbf{R}_{\mathrm{x}}=\begin{bmatrix}1 & 0 & 0 & 0\\ 0 & \cos(\theta_{\mathrm{a}}) & \sin(\theta_{\mathrm{a}}) & 0\\ 0 & -\sin(\theta_{\mathrm{a}}) & \cos(\theta_{\mathrm{a}}) & 0\\ 0 & 0 & 0 & 1\end{bmatrix}. \tag{4.1}$$

Second, the insert coordinate system is rotated about the $\mathbf{Z}_{\mathrm{i}}$ axis by axial angle $\theta_{\mathrm{r}}$. The rotation matrix is

$$\mathbf{R}_{\mathrm{z}}=\begin{bmatrix}\cos(\theta_r) & \sin(\theta_r) & 0 & 0\\ -\sin(\theta_r) & \cos(\theta_r) & 0 & 0\\ 0 & 0 & 1 & 0\\ 0 & 0 & 0 & 1\end{bmatrix}. \tag{4.2}$$

Then, the insert coordinate system is moved to the origin $\mathbf{O}_{\mathrm{t}}$ of the tool coordinate system by tool radius $r$. The movement matrix is

$$\mathbf{T}_{\mathrm{m}}=\begin{bmatrix}1 & 0 & 0 & r\\ 0 & 1 & 0 & 0\\ 0 & 0 & 1 & 0\\ 0 & 0 & 0 & 1\end{bmatrix}. \tag{4.3}$$

At last, the equivalent transformation matrix between the tool coordinate system $\mathbf{X}_{\mathrm{t}}$ - $\mathbf{Y}_{\mathrm{t}}$ - $\mathbf{Z}_{\mathrm{t}}$ - $\mathbf{O}_{\mathrm{t}}$ and the insert coordinate system $\mathbf{X}_{\mathrm{i}}$ - $\mathbf{Y}_{\mathrm{i}}$ - $\mathbf{Z}_{\mathrm{i}}$ - $\mathbf{O}_{\mathrm{i}}$ is derived as

$$ {}^{t}\mathbf{M}_{r} = \mathbf{R}_{x} \cdot \mathbf{R}_{z} \cdot \mathbf{T}_{m} = \begin{bmatrix} \cos(\theta_{r}) & \sin(\theta_{r}) \cdot \cos(\theta_{a}) & \sin(\theta_{r}) \cdot \sin(\theta_{a}) & r \\ -\sin(\theta_{r}) & \cos(\theta_{r}) \cdot \cos(\theta_{a}) & \sin(\theta_{a}) \cdot \cos(\theta_{r}) & 0 \\ 0 & -\sin(\theta_{a}) & \cos(\theta_{a}) & 0 \\ 0 & 0 & 0 & 1 \end{bmatrix}. \quad (4.4) $$

## 4.2 Formulation of equations of the flank wear land width on the side cutting edge

In machining with an indexable face mill, flank wear occurs on the insert's side and corner cutting edges. Here, equations of the width of the flank wear land on the side cutting edge are derived. Suppose the unit normal of the rake face is ${}^{i}\mathbf{i}_{r}$, and the unit normal of the flank face is ${}^{i}\mathbf{i}_{s}$ in the insert coordinate system (see Fig. 4.3). Then, the parametric equations of the two planes in the insert coordinate system can be expressed. The insert's side cutting edge is the intersecting line between the rake and the flank faces, and the angle between the rake and the flank faces is the cutting angle of the insert. The cutting angle is calculated by the supplementary to the angle between vectors ${}^{i}\mathbf{i}_{r}$ and ${}^{i}\mathbf{i}_{s}$. The clearance angle $\beta$ is the complement angle to the cutting angle of the insert.

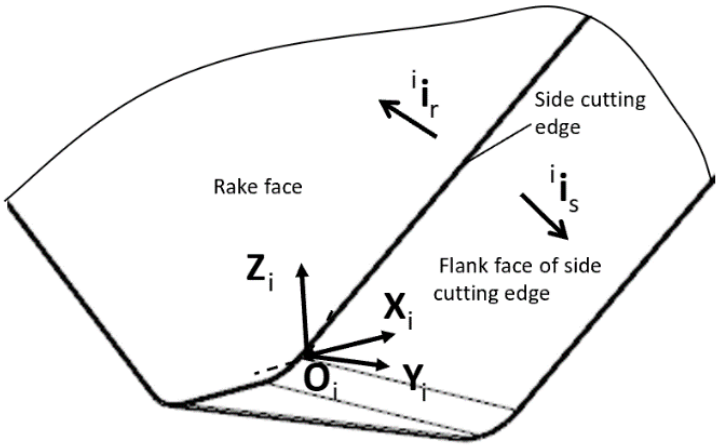


**Figure 2.19 The unit normal vectors of the rake and the flank faces are plotted.**

The unit normal vectors of the rake and the flank faces of the side cutting edge in the insert coordinate system are derived as

$$^{i}\mathbf{i}_s = \left[\sin(k)\cdot\cos(\beta) \quad \sin(\beta) \quad -\cos(k)\cdot\cos(\beta)\right]', \tag{4.5}$$

$$^{i}\mathbf{i}_r = \left[0 \quad -1 \quad 0\right]'. \tag{4.6}$$

According to the transformation matrix in equation (4.4), the unit normal vectors of the rake and the flank faces in the tool coordinate system can be found as

$$ {}^{\mathrm{t}}\mathbf{i}_{\mathrm{s}} = {}^{\mathrm{t}}\mathbf{M}_{\mathrm{r}} \cdot {}^{\mathrm{i}}\mathbf{i}_{\mathrm{s}} = \begin{bmatrix} A_1 \\ B_1 \\ C_1 \end{bmatrix}, \tag{4.7} $$

where

$$ \begin{aligned} A_1 &= -\sin(\theta_{\mathrm{a}}) \cdot \sin(\theta_{\mathrm{r}}) \cdot \cos(\beta) \cdot \cos(k) + \cos(\theta_{\mathrm{r}}) \cdot \cos(\beta) \cdot \sin(k) + \cos(\theta_{\mathrm{a}}) \cdot \sin(\theta_{\mathrm{r}}) \cdot \sin(\beta), \\ B_1 &= -\sin(\theta_{\mathrm{r}}) \cdot \cos(\beta) \cdot \sin(k) + \cos(\theta_{\mathrm{r}}) \cdot \cos(\theta_{\mathrm{a}}) \cdot \sin(\beta) - \sin(\theta_{\mathrm{a}}) \cdot \cos(\theta_{\mathrm{r}}) \cdot \cos(\beta) \cdot \cos(k), \\ C_1 &= -\sin(\theta_{\mathrm{a}}) \cdot \sin(\beta) - \cos(\theta_{\mathrm{a}}) \cdot \cos(\beta) \cdot \cos(k). \end{aligned} \tag{4.8} $$

$$ {}^{\mathrm{t}}\mathbf{i}_{\mathrm{r}} = {}^{\mathrm{t}}\mathbf{M}_{\mathrm{r}} \cdot {}^{\mathrm{i}}\mathbf{i}_{\mathrm{r}} = \begin{bmatrix} -\cos(\theta_{\mathrm{a}}) \cdot \sin(\theta_{\mathrm{r}}) \\ -\cos(\theta_{\mathrm{a}}) \cdot \cos(\theta_{\mathrm{r}}) \\ \sin(\theta_{\mathrm{a}}) \end{bmatrix} = \begin{bmatrix} A_2 \\ B_2 \\ C_2 \end{bmatrix}. \tag{4.9} $$

The intersection of the side cutting edge and the bottom cutting edge is assumed as point ${}^{\mathrm{t}}\mathbf{O}$, which is on both the rake and the flank faces in the tool coordinate system. The distance between this point and the tool axis $\mathbf{Z}_{\mathrm{t}}$ is the tool radius $r$. Thus, its coordinates in the tool coordinate system are

$$ {}^{\mathrm{t}}\mathbf{O} = \begin{bmatrix} x_0 & y_0 & z_0 \end{bmatrix} = \begin{bmatrix} r & 0 & 0 \end{bmatrix}. \tag{4.10} $$

Thus, the equation of the flank face in the tool coordinate system is

$$ A_1 \cdot (x - r) + B_1 \cdot y + C_1 \cdot z = 0, \tag{4.11} $$

and the equation of the rake face is

$$A_2 \cdot (x - r) + B_2 \cdot y + C_2 \cdot z = 0 . \tag{4.12}$$

Suppose the axial depth of cut in machining is $h$. The flank wear occurs on the original side cutting edge from the bottom to the top end with a height of $h$, and a flank wear land with a new cutting edge is generated (see Fig. 4.4). In the cutter coordinate system, a plane parallel to the $\mathbf{X}_t$ - $\mathbf{Y}_t$ plane and with a height of $h$ is generated. This plane intersects the flank wear land with a circle, and the radius of the circle is $R_w$. The circle intersects with the flank face at point $\mathbf{P}_{sw}$ (see Fig. 4.5). Therefore, point $\mathbf{P}_{sw}$ can be computed below.

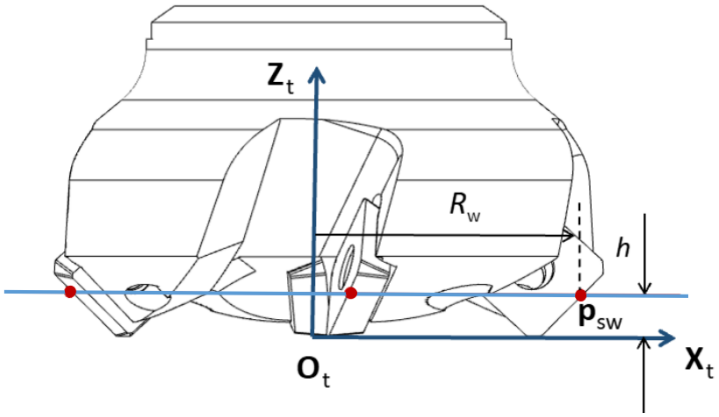


**Figure 2.20 The circle of the flank wear land intersects the land at point $\mathbf{P}_{sw}$.**

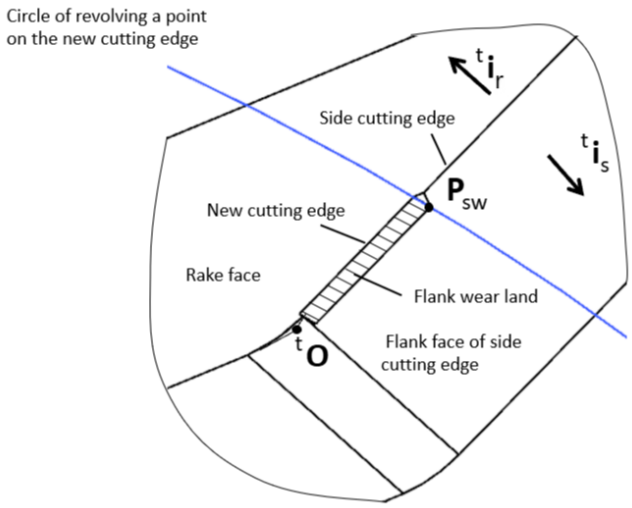


**Figure 2.21 The flank wear land of the side cutting edge is plotted.**

Point $\mathbf{P}_{sw}$ is on the flank face. Its $z$ coordinate in the tool coordinate system is $h$, and the relationship between its $x$ and $y$ coordinates can be represented as

$$A_1 \cdot (x_{sw} - r) + B_1 \cdot y_{sw} + C_1 \cdot z_{sw} = 0, \tag{4.13}$$

$$x_{sw} = -\frac{B_1}{A_1} \cdot y_{sw} + \frac{A_1 \cdot r - C_1 \cdot h}{A_1} = D_1 \cdot y_{sw} + E_1. \tag{4.14}$$

where parameters $D_1$ and $E_1$ are shown as

$$D_1 = -\frac{B_1}{A_1}, \tag{4.15}$$

$$E_1 = \frac{A_1 \cdot r - C_1 \cdot h}{A_1}. \tag{4.16}$$

Point $\mathbf{P}_{sw}$ is also on the circle at the height of $h$; the radius of the circle is $R_w$. The relationship between its coordinates can also be represented as follows.

$$x_{sw}^2 + y_{sw}^2 = R_w^2, \tag{4.17}$$

$$\left(D_1 \cdot y_{sw} + E_1\right)^2 + y_{sw}^2 = R_w^2, \tag{4.18}$$

$$\left(D_1 + 1\right) \cdot y_{sw}^2 + 2 \cdot D_1 \cdot E_1 \cdot y_{sw} + E_1^2 - R_w^2 = 0, \tag{4.19}$$

$$F_1 \cdot y_{sw}^2 + G_1 \cdot y_{sw} + H_1 = 0, \tag{4.20}$$

where parameters $F_1$, $G_1$, and $H_1$ are shown as

$$F_1 = D_1 + 1, \tag{4.21}$$

$$G_1 = 2 \cdot D_1 \cdot E_1, \tag{4.22}$$

$$H_1 = E_1^2 - R_w^2. \tag{4.23}$$

Combining the equations from (4.13) to (4.23), two sets of the coordinates of point $\mathbf{P}_{sw}$ are solved. The result is given below. One of the solutions is selected as the $x$ and $y$ coordinates of point $\mathbf{P}_{sw}$ according to the geometric model.

$$\begin{cases} y_{\mathrm{sw1}} = \dfrac{-G_1 + \sqrt{G_1^2 - 4 \cdot F_1 \cdot H_1}}{2 \cdot F_1} \\ x_{\mathrm{sw1}} = D_1 \cdot y_{\mathrm{sw1}} + E_1 \end{cases} \tag{4.24}$$

$$\begin{cases} y_{\mathrm{sw2}} = \dfrac{-G_1 - \sqrt{G_1^2 - 4 \cdot F_1 \cdot H_1}}{2 \cdot F_1} \\ x_{\mathrm{sw2}} = D_1 \cdot y_{\mathrm{sw2}} + E_1 \end{cases} \tag{4.25}$$

Based on the mechanism of measuring the width of the flank wear land, the width is the vertical distance from the intersection point $\mathbf{P}_{\mathrm{sw}}$ to the rake face. The width of the flank wear land can be calculated as

$$\mathrm{L}_{\mathrm{sVB}} = \frac{\left| A_2 \cdot \left( x_{\mathrm{sw}} - r \right) + B_2 \cdot y_{\mathrm{sw}} + C_2 \cdot h \right|}{\sqrt{A_2{}^2 + B_2{}^2 + C_2{}^2}}. \tag{4.26}$$

## 4.3 Formulation of equations of the flank wear land width on the corner cutting edge

Flank wear occurs on the corner cutting edge, but the equation of the width of the flank wear land is different from that of the flank wear on the side cutting edge. The equation of the flank wear on the corner cutting edge is derived here. Assume a point $\mathbf{E}_{\mathrm{r}}$ on the corner cutting edge shown in Fig. 4.6, and its parametric equation in the insert coordinate system is

$$ {}^{\mathrm{i}}\mathbf{E}_{\mathrm{r}} = \begin{bmatrix} x_{\mathrm{l}} \\ y_{\mathrm{l}} \\ z_{\mathrm{l}} \\ 1 \end{bmatrix} = \begin{bmatrix} r_{\mathrm{c}} \cdot \left(\sin\left(\alpha\right) - \tan\left(k/2\right)\right) \\ 0 \\ r_{\mathrm{c}} \cdot \left(1 - \cos\left(\alpha\right)\right) \\ 1 \end{bmatrix}, \tag{4.27} $$

where $r_{\mathrm{c}}$ is the corner radius of the insert, and the angle α determines the coordinates of point $\mathbf{E}_{\mathrm{r}}$.

According to the transformation matrix in equation (4.4), the parametric equation of the corner cutting edge in the cutter coordinate system is

$$ {}^{\mathrm{t}}\mathbf{E}_{\mathrm{r}} = {}^{\mathrm{t}}\mathbf{M}_{\mathrm{r}} \cdot {}^{\mathrm{i}}\mathbf{E}_{\mathrm{r}} = \begin{bmatrix} r_{\mathrm{c}} \cdot \left(\cos\left(\theta_{\mathrm{r}}\right) \cdot \left(\sin\left(\alpha\right) - \tan\left(k/2\right)\right) + \sin\left(\theta_{\mathrm{r}}\right) \cdot \sin\left(\theta_{\mathrm{a}}\right) \cdot \left(1 - \cos\left(\alpha\right)\right)\right) + r \\ r_{\mathrm{c}} \cdot \left(-\sin\left(\theta_{\mathrm{r}}\right) \cdot \left(\sin\left(\alpha\right) - \tan\left(k/2\right)\right) + \cos\left(\theta_{\mathrm{r}}\right) \cdot \sin\left(\theta_{\mathrm{a}}\right) \cdot \left(1 - \cos\left(\alpha\right)\right)\right) \\ r_{\mathrm{c}} \cdot \cos\left(\theta_{\mathrm{a}}\right) \cdot \left(1 - \cos\left(\alpha\right)\right) \\ 1 \end{bmatrix} = \begin{bmatrix} x_{\mathrm{r}} \\ y_{\mathrm{r}} \\ z_{\mathrm{r}} \\ 1 \end{bmatrix}. \tag{4.28} $$

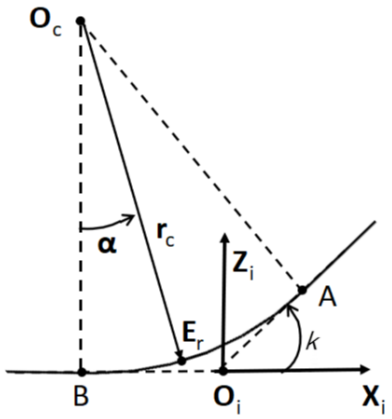


**Figure 2.22 The insert corner cutting edge is plotted in the insert coordinate system.**

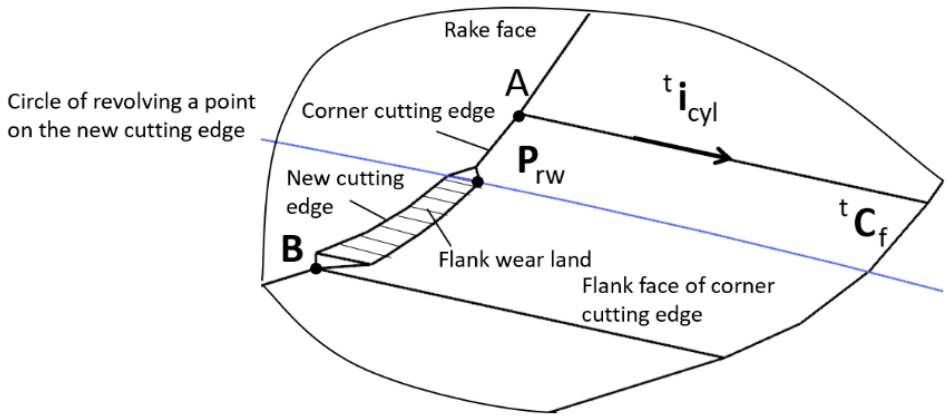


**Figure 2.23 The flank wear land on the corner cutting edge is plotted.**

Fig. 4.7 shows the design of the insert corner cutting edge. It is an intersection arc between the rake face and the flank face of the corner cutting edge. This flank face is a cylindrical surface, and its generatrix is the intersection between the flank faces of the side cutting edge and the bottom cutting edge. The unit normal of the flank face of the bottom cutting edge is $^{i}\mathbf{i}_{b}$:

$$^{i}\mathbf{i}_{b} = \begin{bmatrix} 0 & \sin(\beta) & -\cos(\beta) \end{bmatrix}'. \tag{4.29}$$

The generatrix of the flank face of the corner cutting edge in the insert coordinate system can be calculated as follows.

$$^{t}\mathbf{i}_{cyl} = {}^{t}\mathbf{M}_{r} \cdot {}^{i}\mathbf{i}_{cyl} = {}^{t}\mathbf{M}_{r} \cdot {}^{i}\mathbf{i}_{s} \cdot {}^{i}\mathbf{i}_{b} = \begin{bmatrix} a \\ b \\ c \end{bmatrix}, \tag{4.30}$$

where

$$
\begin{aligned}
a &= \cos(\theta_a)\cdot\sin(\theta_r)\cdot\left(\cos(\beta)\right)^2\cdot\sin(k)-\cos(\beta)\cdot\sin(\beta)\cdot\Big(\big(1-\cos(k)\big)\cdot\cos(\theta_r)-\sin(\theta_a)\cdot\sin(\theta_r)\cdot\sin(k)\Big),\\
b &= \cos(\theta_a)\cdot\cos(\theta_r)\cdot\left(\cos(\beta)\right)^2\cdot\sin(k)+\cos(\beta)\cdot\sin(\beta)\cdot\Big(\big(1-\cos(k)\big)\cdot\sin(\theta_r)+\sin(\theta_a)\cdot\cos(\theta_r)\cdot\sin(k)\Big),\\
c &= \cos(\beta)\cdot\sin(k)\cdot\big(\cos(\theta_a)\cdot\sin(\beta)-\sin(\theta_a)\cdot\cos(\beta)\big).
\end{aligned}
\tag{4.31}
$$

The parametric equation of the flank face of the corner cutting edge in the tool coordinate system is

$$
{}^{t}\mathbf{C}_f=\begin{bmatrix}x\\y\\z\end{bmatrix}'=\begin{bmatrix}x_r+a\cdot t\\y_r+b\cdot t\\z_r+c\cdot t\end{bmatrix}'. \tag{4.32}
$$

Suppose the axial depth of cut in machining is $h$. The flank wear occurs on the original corner cutting edge, and a flank wear land is generated with a new cutting edge (see Fig. 4.7). In the cutter coordinate system, a plane parallel to the $\mathbf{X}_t$ - $\mathbf{Y}_t$ plane and with a height of $h$ is generated. This plane intersects the flank wear land with a circle, and the radius of the circle is $R_w$. The circle intersects with the flank face at point $\mathbf{P}_{rw}$. The coordinates of point $\mathbf{P}_{rw}$ can be computed with the following equations.

$$
\begin{cases}
x_{rw}=x_r+a\cdot t\\
y_{rw}=y_r+b\cdot t\\
z_{rw}=z_r+c\cdot t=h\\
x_{rw}^2+y_{rw}^2=R_w{}^2
\end{cases}
\tag{4.33}
$$

First, the $z$ coordinate of point $\mathbf{P}_{rw}$ in the tool coordinate system is $h$, and solve parameter $t$:

$$z_{\mathrm{rw}} = z_{\mathrm{r}} + c \cdot t = r_{\mathrm{c}} \cdot \cos\left(\theta_{\mathrm{a}}\right) \cdot \left(1 - \cos\left(\alpha\right)\right) + c \cdot t = h\,, \tag{4.34}$$

$$c \cdot t = h + r_{\mathrm{c}} \cdot \cos\left(\theta_{\mathrm{a}}\right) \cdot \cos\left(\alpha\right) - r_{\mathrm{c}} \cdot \cos\left(\theta_{\mathrm{a}}\right), \tag{4.35}$$

$$t = \frac{r_{\mathrm{c}} \cdot \cos\left(\theta_{\mathrm{a}}\right)}{c} \cdot \cos\left(\alpha\right) + \frac{h - r_{\mathrm{c}} \cdot \cos\left(\theta_{\mathrm{a}}\right)}{c} = d \cdot \cos\left(\alpha\right) + e\,, \tag{4.36}$$

where parameters *d* and e are shown as

$$d = \frac{r_{\mathrm{c}} \cdot \cos\left(\theta_{\mathrm{a}}\right)}{c}\,, \tag{4.37}$$

$$e = \frac{h - r_{\mathrm{c}} \cdot \cos\left(\theta_{\mathrm{a}}\right)}{c}\,. \tag{4.38}$$

Second, the *x* coordinate of point $\mathbf{P}_{\mathrm{rw}}$ is converted to the coordinate in the tool coordinate system with equation (4.4).

$$x_{\mathrm{r}} = r_{\mathrm{c}} \cdot \left( \cos\left(\theta_{\mathrm{r}}\right) \cdot \left( \sin\left(\alpha\right) - \tan\left(\frac{k}{2}\right) \right) + \sin\left(\theta_{\mathrm{r}}\right) \cdot \sin\left(\theta_{\mathrm{a}}\right) \cdot \left(1 - \cos\left(\alpha\right)\right) \right) + r\,, \tag{4.39}$$

$$x_{\mathrm{r}} = r_{\mathrm{c}} \cdot \cos\left(\theta_{\mathrm{r}}\right) \cdot \sin\left(\alpha\right) - r_{\mathrm{c}} \cdot \sin\left(\theta_{\mathrm{r}}\right) \cdot \sin\left(\theta_{\mathrm{a}}\right) \cdot \cos\left(\alpha\right) - r_{\mathrm{c}} \cdot \cos\left(\theta_{\mathrm{r}}\right) \cdot \tan\left(\frac{k}{2}\right) + r_{\mathrm{c}} \cdot \sin\left(\theta_{\mathrm{r}}\right) \cdot \sin\left(\theta_{\mathrm{a}}\right) + r, \tag{4.40}$$

$$x_{\mathrm{r}} = f \cdot \sin(\alpha) + g \cdot \cos(\alpha) + h, \tag{4.41}$$

where parameters *f*, *g*, and *h* are shown as

$$f = r_{\mathrm{c}} \cdot \cos(\theta_{\mathrm{r}}), \tag{4.42}$$

$$g = -r_{\mathrm{c}} \cdot \sin(\theta_{\mathrm{r}}) \cdot \sin(\theta_{\mathrm{a}}), \tag{4.43}$$

$$h = -r_{\mathrm{c}} \cdot \cos(\theta_{\mathrm{r}}) \cdot \tan\left(\frac{k}{2}\right) + r_{\mathrm{c}} \cdot \sin(\theta_{\mathrm{r}}) \cdot \sin(\theta_{\mathrm{a}}) + r\,. \tag{4.44}$$

Combining equation (4.33), the *x* coordinate of $\mathbf{P}_{\mathrm{rw}}$ in the tool coordinate system can be represented as follows.

$$\begin{aligned} x_{\mathrm{rw}} &= x_{\mathrm{r}} + a \cdot t = f \cdot \sin(\alpha) + g \cdot \cos(\alpha) + h + a \cdot t \\ &= f \cdot \sin(\alpha) + g \cdot \cos(\alpha) + h + a \cdot (d \cdot \cos(\alpha) + e) \\ &= f \cdot \sin(\alpha) + (g + a \cdot d) \cdot \cos(\alpha) + h + a \cdot e \end{aligned} \tag{4.45}$$

Then, the *y* coordinate of point $\mathbf{P}_{\mathrm{rw}}$ is converted to the coordinate in the tool coordinate system with equation (4.28).

$$y_{\mathrm{r}} = r_{\mathrm{c}} \cdot \left(-\sin(\theta_{\mathrm{r}}) \cdot (\sin(\alpha) - \tan(k/2)) + \cos(\theta_{\mathrm{r}}) \cdot \sin(\theta_{\mathrm{a}}) \cdot (1 - \cos(\alpha))\right), \tag{4.46}$$

$$y_{\mathrm{r}} = -r_{\mathrm{c}} \cdot \sin\left(\theta_{\mathrm{r}}\right) \cdot \sin\left(\alpha\right) - r_{\mathrm{c}} \cdot \cos\left(\theta_{\mathrm{r}}\right) \cdot \sin\left(\theta_{\mathrm{a}}\right) \cdot \cos\left(\alpha\right) + r_{\mathrm{c}} \cdot \sin\left(\theta_{\mathrm{r}}\right) \cdot \tan\left(\frac{k}{2}\right) + r_{\mathrm{c}} \cdot \cos\left(\theta_{\mathrm{r}}\right) \cdot \sin\left(\theta_{\mathrm{a}}\right), \tag{4.47}$$

$$y_{\mathrm{r}} = i \cdot \sin\left(\alpha\right) + j \cdot \cos\left(\alpha\right) + k, \tag{4.48}$$

where parameters $i$, $j$ and $k$ are shown as

$$i = -r_{\mathrm{c}} \cdot \sin\left(\theta_{\mathrm{r}}\right), \tag{4.49}$$

$$j = -r_{\mathrm{c}} \cdot \cos\left(\theta_{\mathrm{r}}\right) \cdot \sin\left(\theta_{\mathrm{a}}\right), \tag{4.50}$$

$$k = r_{\mathrm{c}} \cdot \sin\left(\theta_{\mathrm{r}}\right) \cdot \tan\left(\frac{k}{2}\right) + r_{\mathrm{c}} \cdot \cos\left(\theta_{\mathrm{r}}\right) \cdot \sin\left(\theta_{\mathrm{a}}\right), \tag{4.51}$$

Similarly, the $y$ coordinate of $\mathbf{P}_{\mathrm{rw}}$ in the tool coordinate system is shown below.

$$\begin{aligned} y_{\mathrm{rw}} &= y_{\mathrm{r}} + b \cdot t = i \cdot \sin\left(\alpha\right) + j \cdot \cos\left(\alpha\right) + k + b \cdot t \\ &= i \cdot \sin\left(\alpha\right) + j \cdot \cos\left(\alpha\right) + k + b \cdot \left(d \cdot \cos\left(\alpha\right) + e\right) \\ &= i \cdot \sin\left(\alpha\right) + \left(j + b \cdot d\right) \cdot \cos\left(\alpha\right) + k + b \cdot e \end{aligned} \tag{4.52}$$

At last, point $\mathbf{P}_{\mathrm{rw}}$ is also on the circle at the height of $h$; the radius of the circle is $R_{\mathrm{w}}$. According to equation (4.33), parameter $\alpha$ can be solved by the following equations using computer aid. The

coordinates of intersection point $\mathbf{P}_{rw}$ in the tool coordinate system is solved by substituting parameter $\alpha$ into equation (4.45) and (4.52). Also, the $z$ coordinate of point $\mathbf{P}_{rw}$ in the tool coordinate system is the height $h$.

The vertical distance from point $\mathbf{P}_{rw}$ to the rake face is the width of the flank wear land, which can be calculated as

$$\mathrm{L}_{\mathrm{rVB}} = \frac{\left|A_2 \cdot \left(x_{\mathrm{rw}} - r\right) + B_2 \cdot y_{\mathrm{rw}} + C_2 \cdot h\right|}{\sqrt{A_2^{\,2} \cdot + B_2^{\,2} \cdot + C_2^{\,2}}} . \tag{4.53}$$

# Chapter 5 Experiments and Applications

## 5.1 Objectives of the experiment

With OMM of cutting tools, it is quick to measure the tool radius at a height with the laser tool setter in machining. However, the tool flank wear is irregular, and the widths of the flank wear land at several locations are more significant than those at the other locations. The flank wear with larger land widths deteriorates quickly, resulting in tool failure. The measurement time is extended if the tool is measured at many heights. Therefore, the locations along the tool axis should be optimized so that the measured radius can represent the flank wear and the measurement time is short. The first objective of experiments is to optimize the heights for tool radius measurement. It includes two steps:

1. The images of the flank wear land are collected regularly with a microscope until the cutter fails. The widths of the flank wear land are measured on the images and compared to determine the flank wear pattern.

2. The heights with large flank wears and failure are determined as the heights for measuring tool radius, and the width threshold of the flank wear land is determined for tool condition monitoring.

In the previous chapters, the geometric relationship between tool radius and flank wear width of the indexable face mill is established. Thus, the other objective of the experiment is to verify this geometric relationship. The tool radius is measured at different preset heights with a laser tool setter. The corresponding flank wear land widths are calculated. Meanwhile, the actual flank wear land widths at these heights are measured on the images collected with the microscope.

The calculated land widths and actual land widths are compared to verify the equations of the width of the flank wear land.

After the measurement positions are determined and the geometric relationship is verified for the indexable face mill, the application experiment of the tool condition monitoring in this thesis should be conducted as follows. The indexable face mill is measured for radius with a laser tool setter at the optimized heights. When a tool radius is measured at a height, the width of the corresponding flank wear land is calculated using the geometric relationship between tool radius and flank wear land width. The land widths at all heights are calculated and compared to the threshold for tool condition monitoring. If a land width is larger than the threshold, the milling tool is considered to be invalid. The flank wear land of the inserts on the milling tool should be observed with the microscope to verify it has failed.

## 5.2 Experimental setup

The experiments are conducted to achieve the objectives. Here, the experimental setup is introduced. An indexable face mill of model TSE12 is adopted, with two cemented carbide inserts (see Fig. 5.1). The workpiece material is 2Cr13 stainless steel. The tool cuts the material with coolant. Fig. 5.2 shows the experimental setup. A three-axis CNC milling machine is employed, and a laser tool setter is set up on the machine table. A workpiece with 103 by 103 by 30 mm is clamped with a vise as shown in Fig. 5.3.


**Figure 2.24 The TSE12 indexable face mill has two inserts.**

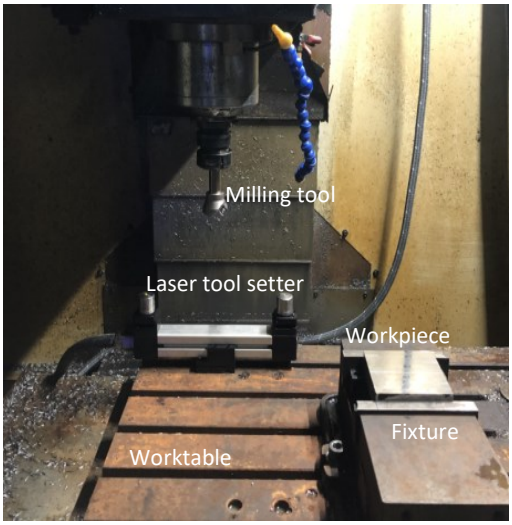


**Figure 2.25 The experimental environment is set up.**

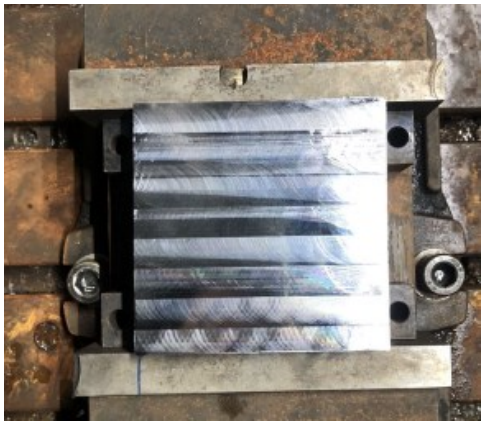

**Figure 2.26 The 2Cr13 stainless steel workpiece is fixed in a vise.**

The tool cuts the workpiece with a feed of 0.08 mm/tooth, cutting speed of 180 m/min, and cutting depth of 1 mm. The tool cuts the workpiece back and forth, and a cut refers to a path from left to right of the workpiece. In tool preparation, the new inserts are manually adjusted with an off-machine tool setter to ensure the tool radius and length difference of the tool nose are within 0.01 mm. The tool parameter values are listed in Table 5.1.

**Table 2.3 The parameter values of the TSE12 indexable face mill.**

| Tool radius $r$ | Axial angle $\theta_a$ | Radial angle $\theta_r$ | Entering angle $k$ | Clearance angle $\beta$ |
|---|---|---|---|---|
| 16.026 mm | 9° | 15° | 45° | 20° |

There are five preset heights of measurement $h$ in the tool coordinate system, which are determined as 0.1, 0.2, 0.4, 0.65, and 0.9 mm. The heights correspond to five points, $\mathbf{P}_1$, $\mathbf{P}_2$, $\mathbf{P}_3$, $\mathbf{P}_4$, and $\mathbf{P}_5$, on the insert cutting edge. Points $\mathbf{P}_1$ and $\mathbf{P}_2$ are located on the corner cutting edge, and points $\mathbf{P}_3$, $\mathbf{P}_4$ and $\mathbf{P}_5$ are located on the side cutting edge. Before machining, the tool radii at the five heights are measured with the laser tool setter. After two cuts, the tool radii are measured with the laser tool setter before removing the tool from the spindle and measuring the widths $V_B$ of the flank wear land with the microscope. In measuring the inserts, the sight direction is parallel to the insert rake face and perpendicular to the cutting edge (see Fig. 5.4).

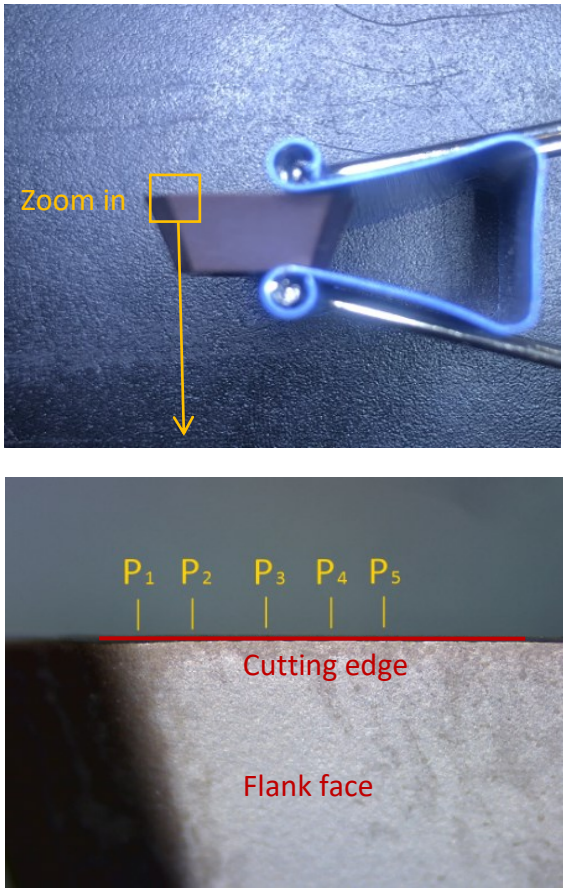


**Figure 2.27 The setting of measuring the flank wear land with the microscope is shown.**

## 5.3 Determination of flank wear pattern and measurement heights

In the experiment, after two cuts, the tool is unloaded from the machine spindle, and the flank wear of the two inserts is examined under a microscope. The images of the flank wear are saved, and the widths of the flank wear land are measured at the five points in each image. There are eight cuts in total, and four flank wear images are shown in Figs. 5.5 to 5.8. Each figure includes two images of flank wear on inserts A and B after two cuts. From the first cut to the sixth cut, the flank wear gets larger, but chipping does not occur. It is ready to see that chipping occurs on the cutting edges of inserts A and B after eight cuts, and the tool fails.

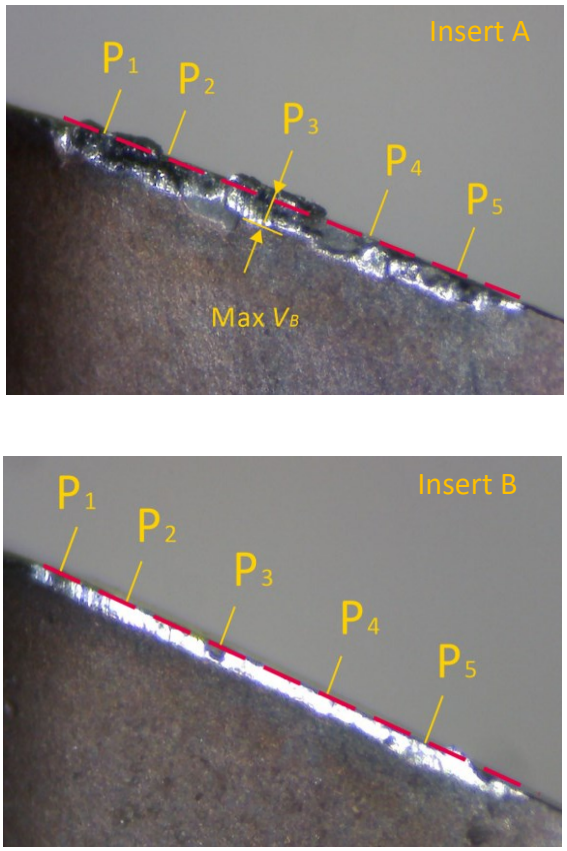


**Figure 2.28 The flank wear images of inserts A and B in the 1st and 2nd cuts are displayed.**

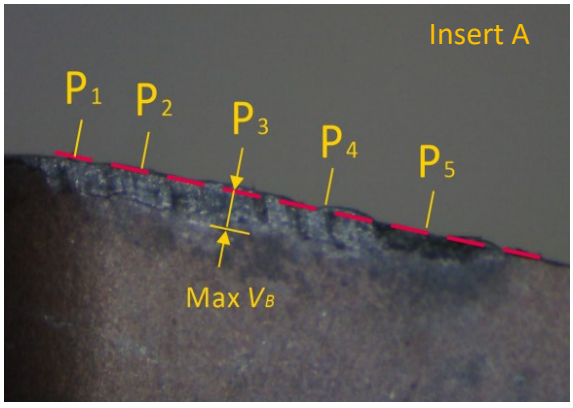

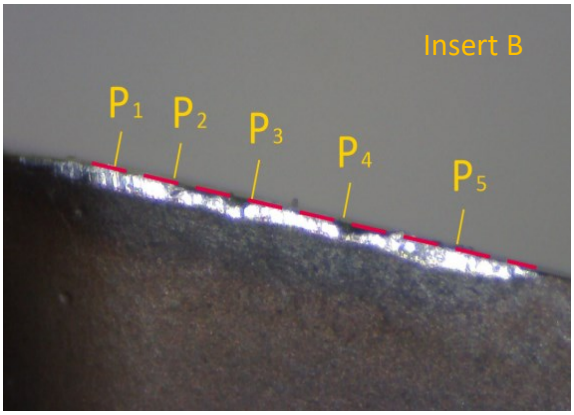


**Figure 2.29 The flank wear images of inserts A and B in the 3rd and 4th cuts are displayed.**

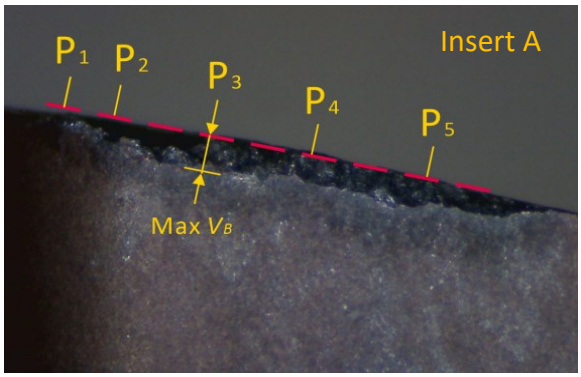


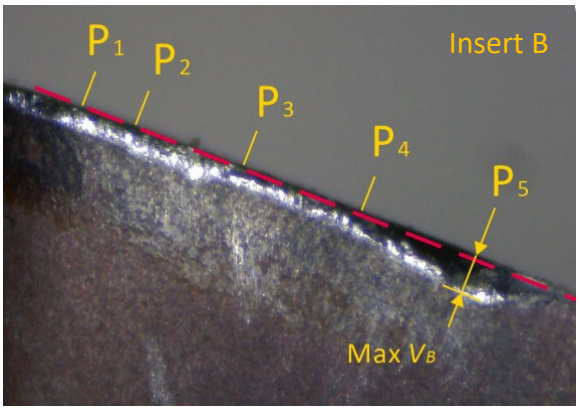


**Figure 2.30 The flank wear images of inserts A and B in the 5th and 6th cuts are displayed.**

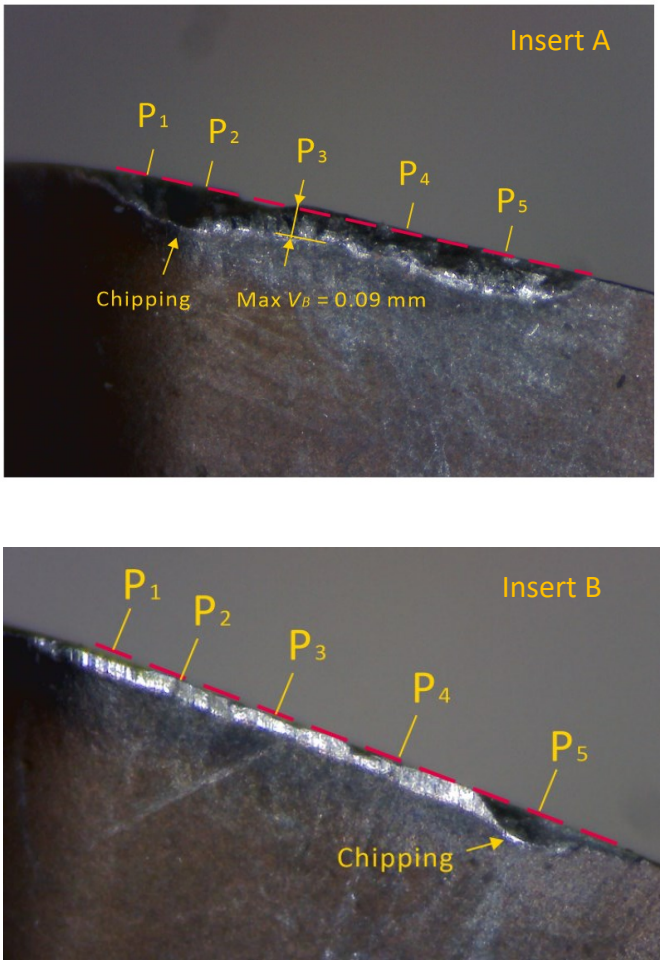


**Figure 2.31 The flank wear images of inserts A and B in the 7th and 8th cuts are displayed.**

Comparing the flank wear of the two inserts (A and B) in the first four cuts (see Figs. 5.5 and 5.6), the flank wear of insert B is relatively smaller than that of insert A. The flank wear land of insert B is in white, which is the workpiece material sticking on the flank wear. Insert B has little wear, while insert A has larger flank wear. At point $\mathbf{P}_3$, the width of the flank wear land is the maximum. Therefore, the flank wear of insert A is larger than that of insert B. In Fig. 5.7, the maximum flank wear occurs at point $\mathbf{P}_3$ of insert A, but the same amount of flank wear occurs at point $\mathbf{P}_5$ of insert B after six cuts. In Fig. 5.8, chipping occurs between points $\mathbf{P}_2$ and $\mathbf{P}_3$ of insert A

and $\mathbf{P}_5$ of insert B after eight cuts. Therefore, by comparing all flank wear patterns of inserts A and B, the measurement heights are at $\mathbf{P}_3$ and $\mathbf{P}_5$.

By checking the four results, in addition, chipping does not occur at points $\mathbf{P}_3$ or $\mathbf{P}_5$ in the first three experiments; however, it appears in the fourth experiment. In the third experiment, the inserts are still in the form of flank wear. There is no chipping on the side cutting edge at the points, and the inserts are valid. In the fourth experiment, the flank wear land width at point $\mathbf{P}_3$ is 0.09 mm, and chipping occurs at point $\mathbf{P}_5$ and between points $\mathbf{P}_2$ and $\mathbf{P}_3$. The tool is defective. Thus, the threshold of the flank wear land width is 0.09 mm.

The first objective of the experiment has been achieved that the measurement locations are determined by recognizing the flank wear pattern. The result shows that the measuring heights for the indexable face mill in this experiment are 0.4 mm and 0.9 mm. For the tool condition monitoring, the maximum width of the flank wear land is determined to be 0.09 mm.

## 5.4 Verification of the equations of the flank wear land width

In this experiment, the tool is measured for radius with the laser tool setter before machining and after every two cuts. The tool radii are measured at the five heights, and the tool radius reductions are determined in each measurement. By using the equations of the width, the widths of the flank wear land at the five heights are calculated, which are called predicted land widths $V_B$. Then, the tool is manually measured for the land width with a microscope, and the actual land widths $V_B$ are recorded in each measurement. Each experiment's results are listed in Tables 5.2 to 5.6.

**Table 2.4 The measured tool radii at the five heights of a new tool**

| Positions | $\mathbf{P}_1$ | $\mathbf{P}_2$ | $\mathbf{P}_3$ | $\mathbf{P}_4$ | $\mathbf{P}_5$ |
|---|---|---|---|---|---|
| Tool radius (mm) | 16.089 | 16.230 | 16.424 | 16.655 | 16.887 |

**Table 2.5 The first experiment results in the 1st and 2nd cuts**

| Positions | $\mathbf{P}_1$ | $\mathbf{P}_2$ | $\mathbf{P}_3$ | $\mathbf{P}_4$ | $\mathbf{P}_5$ |
|---|---|---|---|---|---|
| Tool radius (mm) | 16.057 | 16.190 | 16.390 | 16.624 | 16.866 |
| Radius wear (mm) | 0.032 | 0.04 | 0.034 | 0.031 | 0.021 |
| Predicted $V_B$ (mm) | 0.045 | 0.067 | 0.058 | 0.053 | 0.041 |
| Actual $V_B$ (mm) | 0.05 | 0.06 | 0.06 | 0.06 | 0.04 |
| Error in percentage | 10% | 11.7% | 3% | 11.7% | 2.5% |

**Table 2.6 The second experiment results in the 3rd and 4th cuts**

| Positions | $\mathbf{P}_1$ | $\mathbf{P}_2$ | $\mathbf{P}_3$ | $\mathbf{P}_4$ | $\mathbf{P}_5$ |
|---|---|---|---|---|---|
| Tool radius (mm) | 16.054 | 16.190 | 16.378 | 16.620 | 16.860 |
| Radius wear (mm) | 0.035 | 0.04 | 0.046 | 0.035 | 0.027 |
| Predicted $V_B$ (mm) | 0.049 | 0.067 | 0.078 | 0.06 | 0.052 |
| Actual $V_B$ (mm) | 0.05 | 0.06 | 0.07 | 0.06 | 0.06 |
| Error in percentage | 2% | 11.7% | 11.4% | 0 | 13.3% |

**Table 2.7 The third experiment results in the 5th and 6th cuts**

| Positions | $\mathbf{P}_1$ | $\mathbf{P}_2$ | $\mathbf{P}_3$ | $\mathbf{P}_4$ | $\mathbf{P}_5$ |
|---|---|---|---|---|---|
| Tool radius (mm) | 16.049 | 16.179 | 16.377 | 16.604 | 16.843 |
| Radius wear (mm) | 0.04 | 0.051 | 0.047 | 0.051 | 0.044 |
| Predicted $V_B$ (mm) | 0.055 | 0.087 | 0.08 | 0.087 | 0.081 |
| Actual $V_B$ (mm) | 0.05 | 0.08 | 0.08 | 0.08 | 0.08 |
| Error in percentage | 10% | 7.5% | 0 | 8.8% | 13.8% |

**Table 2.8 The fourth experiment results in the 7th and 8th cuts**

| Positions | $\mathbf{P}_1$ | $\mathbf{P}_2$ | $\mathbf{P}_3$ | $\mathbf{P}_4$ | $\mathbf{P}_5$ |
|---|---|---|---|---|---|
| Tool radius (mm) | 16.038 | 16.171 | 16.372 | 16.603 | 16.829 |
| Radius wear (mm) | 0.051 | 0.059 | 0.052 | 0.052 | 0.058 |
| Predicted $V_B$ (mm) | 0.07 | 0.099 | 0.088 | 0.088 | 0.105 |
| Actual $V_B$ (mm) | 0.07 | Chipping | 0.09 | 0.09 | Chipping |
| Error in percentage | 0 | | 2.2% | 2.2% | |

Table 5.3 includes results in the first experiment of the 1st and 2nd cuts. The maximum difference between the predicted and the actual widths of the flank wear land at the five heights is 11.7%. Table 5.4 includes the second experiment results of the 3rd and 4th cuts. The maximum difference between the predicted and the actual land widths at the five heights is 13.3%. Table 5.5 shows the maximum difference of 13.8% in the third experiment. Table 5.6 shows the land width difference at points $\mathbf{P}_1$, $\mathbf{P}_3$ and $\mathbf{P}_4$ are 0%, 2.2% and 2.2%, respectively, in the fourth experiment. Based on the differences between the predicted and the actual land width, the differences are slight. Thus, the equations of the width of the flank wear land formulated in the previous chapter are accurate. The geometric relationship between tool radius and flank wear land width is verified.

For the tool condition monitoring, the threshold of the flank wear land width is 0.09 mm, as shown in Section 5.2. In the first three experiments, the land widths are less than 0.09 mm; the tool is valid. In the fourth experiment, the predicted land width at point $\mathbf{P}_2$ is 0.099 mm, and the predicted land width at point $\mathbf{P}_5$ is 0.105 mm. They are larger than the threshold, and the tool condition can be regarded as defective. Actually, chipping occurs at the two points. Thus, the evaluation is correct.

## 5.5 Applications

This approach is applied to two examples. The flank wear pattern is determined, and the heights of points $\mathbf{P}_3$ and $\mathbf{P}_5$ are taken as measurement locations. The threshold of the flank wear land width is 0.09 mm for tool condition monitoring. Two new TSE12 indexable face milling tools are adopted to cut a workpiece of 2Cr13 stainless steel in the application examples.

For the first tool, the radius of the tool nose $r$ is 16.036 mm. The tool feed rate is 0.08 mm/tooth, and the cutting speed is 180 m/min. In this cutting experiment, machining is stopped after four cuts to measure tool radii at the two optimized heights. The tool radii are measured at heights 0.4 and 0.9 mm of points $\mathbf{P}_3$ and $\mathbf{P}_5$ with the laser tool setter. One of the measured radii is automatically input into the CNC controller for tool path compensation. The tool radii are collected in Table 5.7.

**Table 2.9 The results of machining with the first tool**

| Positions | Initial | | After four cuts | | After eight cuts | |
|---|---|---|---|---|---|---|
| | $\mathbf{P}_3$ | $\mathbf{P}_5$ | $\mathbf{P}_3$ | $\mathbf{P}_5$ | $\mathbf{P}_3$ | $\mathbf{P}_5$ |
| Tool radius (mm) | 16.431 | 16.898 | 16.385 | 16.849 | 16.377 | 16.834 |
| Radius wear (mm) | 0 | 0 | 0.046 | 0.049 | 0.054 | 0.064 |
| Predicted $V_B$ (mm) | 0 | 0 | 0.078 | 0.085 | 0.092 | 0.11 |
| Status | Valid | Valid | Valid | Valid | Invalid | Invalid |

The results show that after four cuts, the land width is predicted as 0.078 mm at point $\mathbf{P}_3$ and 0.085 mm at point $\mathbf{P}_5$. They are less than 0.09 mm, so the tool is valid. After eight cuts, the land width is predicted as 0.092 mm at point $\mathbf{P}_3$ and 0.11 mm at point $\mathbf{P}_5$. Thus, the tool is invalid. The milling tool is removed from the spindle to observe the two inserts' cutting edges. It's found that there is chipping on the side cutting edge of one of the inserts in Figure 5.9, demonstrating the milling tool is already invalid as predicted.

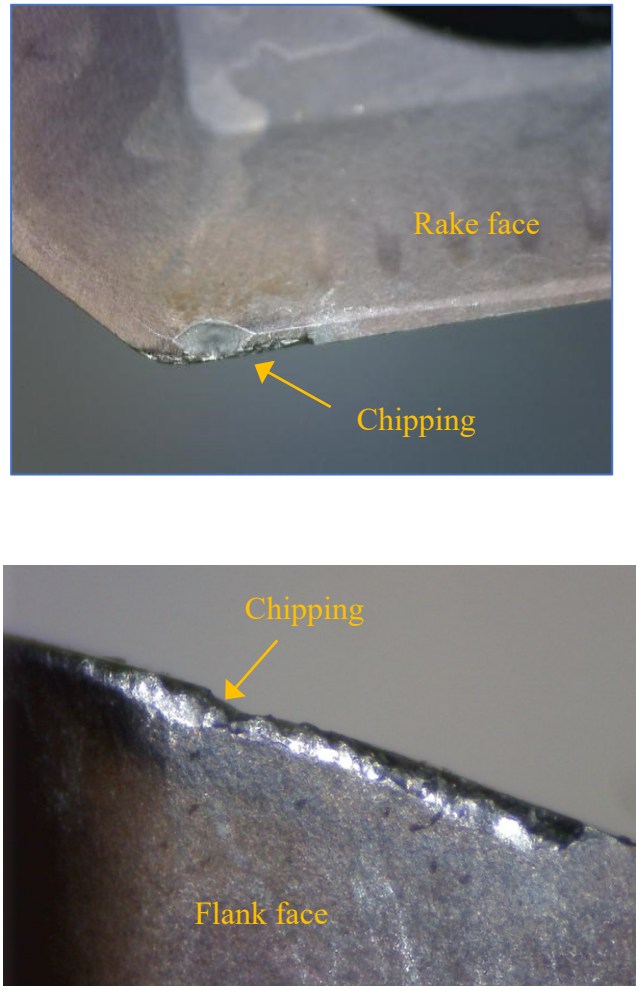


**Figure 2.32 The insert is invalid after eight cuts under the condition of 0.08 mm/tooth feed, 180 m/min speed.**

Another application experiment is conducted for the second tool. The radius of the tool nose *r* is 15.988 mm. The cutting parameters are adjusted so that the tool feed rate is 0.05 mm/tooth, and the cutting speed is 140 m/min. In this cutting experiment, machining is stopped after four cuts to measure tool radii at the two optimized heights: 0.4 and 0.9 mm of points $\mathbf{P}_3$ and $\mathbf{P}_5$. Similarly, one of the measured tool radii is automatically input into the CNC controller for tool path compensation. The results are shown in Table 5.8.

**Table 2.10 The results of machining with the second tool**

| Positions | Initial | | After four cuts | | After eight cuts | |
|---|---|---|---|---|---|---|
| | $\mathbf{P}_3$ | $\mathbf{P}_5$ | $\mathbf{P}_3$ | $\mathbf{P}_5$ | $\mathbf{P}_3$ | $\mathbf{P}_5$ |
| Tool radius (mm) | 16.389 | 16.855 | 16.345 | 16.808 | 16.230 | 16.719 |
| Radius wear (mm) | 0 | 0 | 0.044 | 0.047 | 0.159 | 0.136 |
| Predicted $V_B$ (mm) | 0 | 0 | 0.08 | 0.081 | 0.27 | 0.23 |
| Status | Valid | Valid | Valid | Valid | Invalid | Invalid |

For the second tool, the land width is predicted as 0.08 mm at point $\mathbf{P}_3$ and 0.081 mm at point $\mathbf{P}_5$ after four cuts. They are less than the threshold, so the tool is valid. After eight cuts, the flank wear land width is predicted as 0.27 mm at point $\mathbf{P}_3$ and 0.23 mm at point $\mathbf{P}_5$. Thus, the tool is invalid. Also, the cutting edges of the two inserts are observed by the microscope (see Fig. 5.10). According to the microscopy image, almost the entire cutting edge of the insert had already been broken. The tool is also invalid, as predicted.

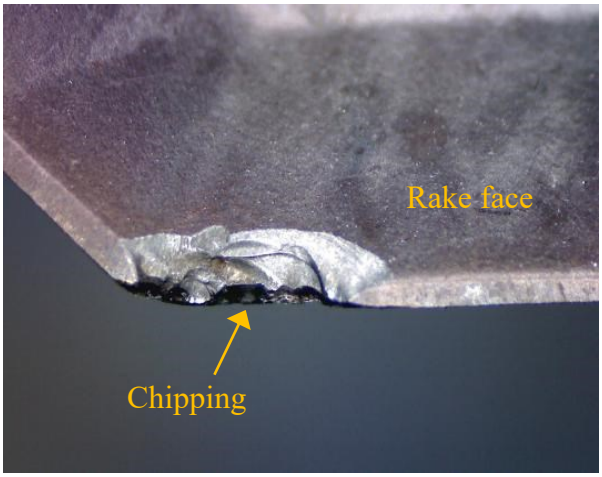

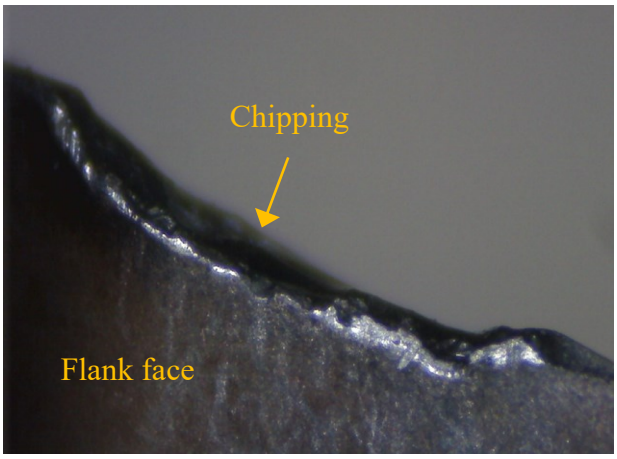


**Figure 2.33 The insert is invalid after eight cuts under the condition of 0.05 mm/tooth feed, 140 m/min speed.**

In the applications, the tool is regularly measured for the radius at the two optimized locations. The measurement time is less. The measured tool radii are input into the CNC controller to compensate for the following machining. At the same time, the tool condition monitoring is conducted, and the tool failure can be predicted.

# Chapter 6 Conclusions

This research proposed a new approach to tool size measurement and flank wear prediction of end-mills. It has addressed the technical challenges of on-machine measurement and tool condition monitoring fusion.

In terms of end-mills modeling, a fillet end-mill is modeled based on the design principles. It focuses on the smoothness of the flank face and considers the relief angle requirement for the flank face on the fillet. In addition, an indexable face mill is modeled accurately. The flank wear land of the insert is also studied to illustrate that it can lead to a reduction of tool radius. Based on the geometric theory, this research initiates the geometric relationship between tool radius and flank wear land width for the indexable face mill. Experiments are conducted to verify the formulated equations. By analyzing the flank wear pattern, the measurement locations are optimized for less measuring time. The width threshold of the flank wear land is also obtained, and the tool condition monitoring is effectively applied in two examples.

The main advantage of this approach is that it can directly measure tool size with a laser tool setter on the machine tool to compensate for the following machining, and at the same time, it can predict flank wear to conduct tool condition monitoring. This approach has great potential to improve machining accuracy and monitor tool conditions to predict the tool life.

# Bibliography

[1] Lee E. S., Lee C. H., and Kim S. C., 2008, Machining accuracy improvement by automatic tool setting and on machine verification, Key Engineering Materials, Vol. 381, pp. 199-202.

[2] Milton V. J., F á bio H. P., Wagner C., and Francisco S., 2015, Influence of feed rate and spindle speed on referencing laser tool-setters, Journal of the Brazilian Society of Mechanical Sciences and Engineering, Vol. 37, pp. 1015-1028.

[3] Shen, Z., Lu, L., Sun, J., Yang, F., Tang, Y., and Xie, Y., 2015, Wear patterns and wear mechanisms of cutting tools used during the manufacturing of chopped carbon fiber. International Journal of Machine Tools and Manufacture, Vol. 97, pp. 1-10.

[4] Marcelo A. R., Amauri H., and Rodrigo H. L., 2016, Tool life and wear mechanisms during Alloy 625 face milling, The International Journal of Advanced Manufacturing Technology, Vol.85, pp.1439-1448.

[5] Kadirgama K., Abou-El-Hossein K. A., Noor M. M., Sharma K. V., and Mohammad B., 2011, Tool life and wear mechanism when machining Hastelloy C-22HS, Wear, Vol. 270, No. 3-4, pp. 258-268.

[6] Naskar A., and Chattopadhyay A. K., 2018, Investigation on flank wear mechanism of CVD and PVD hard coatings in high speed dry turning of low and high carbon steel, Wear, Vol. 396, pp. 98-106.

[7] Šramhauser K., N á prstkov á N., Kraus P., and Marek M., 2018, Comparative study of flank wear, tool life and type of chips for two similar turning inserts from different producers, MATEC Web of Conferences, Vol. 244, 02008.

[8] Arne N., and Hakan W., 1993, Reliability improvement of tool-wear monitoring, CIRP annals, Vol. 42, pp. 63-66.

[9] Niaki F. A., Ulutan D., and Mears L., 2016, Parameter inference under uncertainty in end-milling r-strengthened difficult-to-machine alloy, Journal of Manufacturing Science and Engineering, Vol. 138, 061014

[10] Odedeyi P. B., Abou-El-Hossein K., and Liman M., 2017, An experimental study of flank wear in the end milling of AISI 316 stainless steel with coated carbide inserts, The 6th International Conference on Fracture Fatigue and Wear, Journal of Physics: Conference Series, Vol. 843, 012058.

[11] Wang G., Qian L., and Guo Z., 2013, Continuous tool wear prediction based on Gaussian mixture regression model, The International Journal of Advanced Manufacturing Technology, Vol. 66, No. 9-12, pp. 1921-1929.

[12] Iqbal N., He N., Dar U., and Li L., 2007, Comparison of fuzzy expert system-based strategies of offline and online estimation of flank wear in hard milling process, Expert Systems with Applications, Vol. 33, No. 1, pp. 61-66.

[13] Lu X., Wang F., Jia Z., and Liang S. Y., 2018, The flank wear prediction in micro-milling Inconel 718, Industrial Lubrication and Tribology, Vol.70, pp. 1374-1380.

[14] Roney T., Bauccio A., Shaffer D., Lorson P., Ragai I., Loker D., and Nikhare C., 2018, Acoustic signal analysis for prediction of flank wear during conventional milling, ASME International Mechanical Engineering Congress and Exposition, Vol. 52019, V002T02A004.

[15] Kaya B., Oysu C., and Ertunc H. M., 2011, Force-torque based on-line tool wear estimation system for CNC milling of Inconel 718 using neural networks, Advances in Engineering Software, Vol. 42, No. 3, pp. 76-84.

[16] Singh D., and Rao P. V., 2010, Flank wear prediction of ceramic tools in hard turning, The International Journal of Advanced Manufacturing Technology, Vol.50, pp. 479-493.

[17] Sreeraj P. R., Elias J. V., Manu R., and Mathew J., 2020, Flank wear prediction in tungsten carbide tool using acoustic signal amplitude in conventional turning operation, Proceedings of the Institution of Mechanical Engineers, Part C: Journal of Mechanical Engineering Science, Vol. 235, pp. 4070–4083.

[18] Kuram E., and Ozcelik B., 2017, Optimization of machining parameters during micro-milling of Ti6Al4V titanium alloy and Inconel 718 materials using Taguchi method, Proceedings of the Institution of Mechanical Engineers, Part B: Journal of Engineering Manufacture, Vol. 231, pp. 228-242.

[19] Ozel T., Karpat Y., Figueira L., and Davim J. P., 2009, Modeling of surface finish and tool wear in hard turning of AISI D2 steel using ceramics wiper inserts, Journal of Materials Processing Technology, Vol. 209, pp. 5448-5455.

[20] Choudhury S. K., and Rath S., 2000, In-process tool wear estimation in milling using cutting force model, Journal of Materials Processing Technology, Vol. 99, No. 1, pp. 113-119.

[21] Sarhan A., Sayed R., Nassr A. A., and El-Zahry R. M., 2001, Interrelationships between cutting force variation and tool wear in end-milling, Journal of Materials Processing Technology, Vol. 109, No. 3, pp. 229-235.

[22] Sick B., 2002, Fusion of hard and soft computing techniques in indirect, online tool wear monitoring, IEEE Transactions on Systems, Man, and Cybernetics-Part C: Applications and Reviews, Vol. 32, No. 2, pp. 80-91.

[23] Zhang S., Li J. F., and Wang Y. W., 2012, Tool life and cutting forces in end milling Inconel 718 under dry and minimum quantity cooling lubrication cutting conditions, Journal of Cleaner Production, Vol. 32, pp. 81-87.

[24] Jozic S., Lela B., and Bajic D., 2014, A new mathematical model for flank wear prediction using functional data analysis methodology, Advances in Materials Science and Engineering, Vol. 2014, 138168.

[25] Mohanraj T., and Shanmugam A., 2021, Prediction of tool wear in milling of Inconel 625 using and integrated kurtosis-based algorithm with vibration signals, Journal of Physics: Conference Series, Vol. 1969, 012048.

[26] Hosseini Aghdam B., and Cigeroglu E., 2017, Vibration-based tool wear estimation by using non-stationary Functional Series TARMA (FS-TARMA) models, The International Journal of Advanced Manufacturing Technology, Vol. 93, pp. 1431-1442.

[27] Li B., 2012, A review of tool wear estimation using theoretical analysis and numerical simulation technologies, International Journal of Refractory Metals and Hard Materials, Vol. 35, pp. 143-151.

[28] Zhou J. T., Zhao X., and Gao J., 2019, Tool remaining useful life prediction method based on LSTM under variable working conditions, The International Journal of Advanced Manufacturing Technology, Vol. 104, pp. 4715-4726.

[29] Kwon Y., and Fischer G. W., 2003, A novel approach to quantifying tool wear and tool life measurements for optimal tool management, International Journal of Machine Tools and Manufacture, Vol. 43, No. 4, pp. 359-368.

[30] Adesta, E. Y. T., Al Hazza, M., Riza M., and Agusman D., 2010, Tool life estimation model based on simulated flank wear during high speed hard turning, European Journal of Scientific Research, Vol. 39, pp. 265-278.

[31] Karandikar J., 2019, Machine learning classification for tool life modeling using production shop-floor tool wear data, Procedia Manufacturing, Vol. 34, pp. 446-454.

[32] Lajis M. A., Karim A. N. M., Amin A. K. M. N., Hafiz A. M. K., and Turnad L. G., 2008, Prediction of tool life in end milling of hardened steel AISI D2, European Journal of Scientific Research, Vol. 21, No. 4, pp. 592-602.

[33] Oraby S. E., and Hayhurst D. R., 2004, Tool life determination based on the measurement of wear and tool force ratio variation, International Journal of Machine Tools and Manufacture, Vol. 44, pp. 1261-1269.

[34] Fang Z. X., 2015, Research and application of the cutter geometry on-machine measurement using laser tool setters, Concordia University Master Thesis.

[35] Kurada S., and Bradley C., 1997, A review of machine vision sensors for tool condition monitoring, Computers in Industry, Vol. 34, pp. 55-72.

[36] Ambhore N., Kamble D., Chinchanikar S., and Wayal V., 2015, Tool condition monitoring system: A review, Materials Today: Proceedings, Vol. 2, pp. 3419-3428.